# A Study on 3D Reconstruction for Moving Objects Using High-Speed Active Camera-Projector System

by

Chen Mengjuan

Graduate School of Advanced Science and Engineering
Hiroshima University
September, 2024

# Contents

# List of Figures

# List of Tables

# Chapter 1

# Introduction

## 1.1 Background

In the field of computer vision, 3D measurement has always held a significant position. 3D measurement refers to the process of converting surface information of certain scenes or objects in the real world into discrete geometric data through corresponding algorithms, allowing the three-dimensional information of the surface to be presented in a computer. [1–10]

3D measurement can be classified into contact measurement and non-contact measurement based on whether contact with the surface of the object being measured is required. [11–15] Contact reconstruction technology involves obtaining the surface coordinates of an object by directly contacting it, such as with a coordinate measuring machine or a scanning tunneling microscope. Its advantages include high measurement accuracy, but it has disadvantages such as low efficiency, high cost, and the inability to measure objects with complex surface structures, fragile materials, or soft textures. [16–18]

Non-contact reconstruction technology uses optical or electromagnetic waves to scan or project onto the object being measured to obtain surface information. Non-contact measurement methods include the Stereo Vision Method [19–21], Time of Flight (TOF) Method [22–24], and Structured Light 3D Measurement (Camera-Projector Method) [25, 26, 26, 27]. The Stereo Vision Method uses multiple cameras to capture images of objects, extract features for matching, and then calculate the 3D information of these feature points. However, this method requires objects to have sufficient texture. The TOF Method obtains depth information by emitting infrared light and then calculating the reflection time of the infrared light. This method has lower measurement accuracy but higher measurement speed. The Structured Light Method system consists of a camera and a projector. The projector projects patterns onto the object, which can be points, lines, or planes. The patterns deform when reflected off the object's surface. The camera captures the surface, obtaining a set of encoded feature points. These points are then decoded and matched with the corresponding points on the projection plane and imaging plane. Finally, the 3D data information is calculated based on the system's calibration parameters. This method is known for its high measurement accuracy, speed, and adaptability.

From the above introduction, it is evident that contact-based 3D measurement systems have high setup costs, a limited range of measurable objects, and narrow application areas. In contrast, non-contact 3D measurement primarily relies on physical information such as sound, light, and electricity interacting with the object's surface to obtain 3D information. Non-contact measurement has significant advantages in this regard. Among various non-contact 3D measurement systems, the Camera-Projector technique stands out for its superior accuracy and speed, gradually becoming a major research focus in the field of computer vision.

The 3D measurement of moving objects has garnered significant interest in various fields, including online industrial production inspection [28], robotic arm grasping for moving object navigation [29], motion analysis [30], high-precision positioning in medical robotics [31], and dynamic 3D data acquisition for virtual reality [32]. Currently, the precision and speed of Camera-Projector measurement methods have made significant leaps in the field of 3D measurement. However, existing Camera-Projector methods face significant challenges with 3D reconstruction of high-speed moving objects due to two primary reasons: the static nature of the system, with fixed cameras and projectors, which limits the 3D imaging range, and the lack of dynamic feedback on the target's motion, making it difficult to address reconstruction errors caused by the object's movement.

To overcome the first issue, researchers have proposed various active 3D reconstruction systems. One approach mounts the projector on the end of a robotic arm to improve scanning flexibility; however, its accuracy is limited by the precision of the robotic arm. Another system employs gimbals to drive the projector and camera for scanning, but the system size was significant, and its scanning speed was slow. For the issue of target motion, some researchers have used high-speed projectors for quicker pattern projection and capture. However, the projection speed of multi-tone patterns remains a limiting factor, affecting effectiveness. The fixed field of view (FOV) of both the camera and projector further limits the reconstruction range, making it difficult to accurately reconstruct high-speed moving objects. Other approaches have focused on algorithmic solutions to compensate for measurement errors due to object motion. Although these methods correct some inaccuracies caused by movement, they generally assume uniform motion and are computationally intensive, limiting their utility in real-time applications.

## 1.2 Overview of the research

This paper proposes a novel active 3D reconstruction method for wide-range sensing, which is further combined with a visual feedback-based approach to achieve 3D reconstruction of moving objects. This approach integrates a galvanometer-based tracking system with a dual-galvanometer-based active light-section 3D reconstruction system. Our strategy ensures synchronization between projector scanning, adjustment of the tracking camera's FOV, and modification of the 3D reconstruction camera's FOV, achieved via the precise control of three galvanometers. This setup enables the tracking system to capture the object's motion dynamics and subsequently send this feedback to the active 3D reconstruction system. Consequently, the 3D vision system actively per-

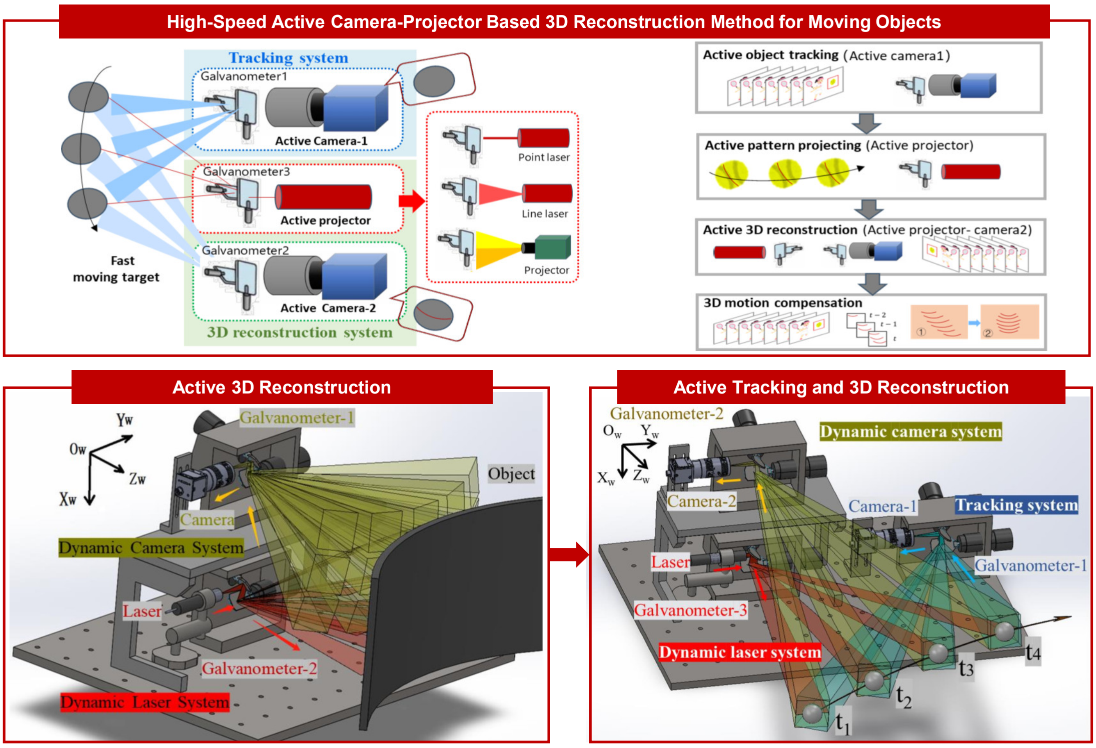

**Figure 1.1: Overview of the research.**

forms laser scanning and captures laser images to facilitate 3D reconstruction of moving objects. Additionally, we have devised a joint calibration technique for both the tracking and active 3D reconstruction systems and introduced a 3D motion error compensation method. Experiments indicate the effectiveness of the proposed method for high-quality 3D reconstruction of moving objects.

## 1.3 Outline of thesis

This thesis is organized as six Chapters, including this introduction.

Chapter 2 summarized related works on 3D reconstruction methods, active camera-projector 3D reconstruction systems and their calibration methods.

In Chapter 3, the concept of active light-section 3D reconstruction method for wide-range sensing is proposed. Besides, a concept of visual-feedback based active 3D reconstruction method for moving objects is also proposed

Chapter 4 introduces the system and algorithms of proposed active light-section 3D reconstruction method that synchronizes laser scanning by switching the field-of-view (FOV) of a camera using multi-galvanometers. Beyond the advanced hardware setup, we establish a comprehensive mathematical model of the system by modeling dynamic camera, dynamic laser, and their combined interaction. Furthermore, since existing calibration methods mainly focus on either dynamic lasers or dynamic cameras and have certain limitations, we propose a novel high-precision and flexible calibration method by constructing an error model and minimizing the objective function.

Chapter 5 introduces the system and algorithms of proposed visual-feedback based active 3D reconstruction method for moving objects that synergistically combines tracking and active 3D reconstruction tailored for moving objects. By integrating visual feedback derived from tracking outcomes, the proposed system ensures that the object maintains a relatively stable relationship with the 3D reconstruction process throughout its movement. The hardware configuration facilitates simultaneous control of tracking, laser scanning, and 3D reconstruction. A comprehensive mathematical model is established to encompass the tracking, active 3D reconstruction, and 3D motion compensation. Furthermore, a precise calibration method based on this mathematical model is detailed.

In Chapter 6, it summarized the contributions of this study and discussed future work.

# Chapter 2

# Related Works

## 2.1 Camera-Projector-based 3D Reconstruction Methods

Camera-projector based 3D reconstruction methods improve the efficiency and accuracy of feature point identification by artificially constructing easily recognizable feature points [33, 34]. The primary approach involves using projection devices to emit light beams with specific patterns onto the target object. These projected patterns are modulated by the surface shape of the object, resulting in specific changes that can be captured by cameras. By establishing spatial geometric relationships based on the equations of the light beams and cameras, the surface depth can be calculated to create a 3D model. This method is known as structured light-based 3D reconstruction. Structured light refers to light beams that can be described using spatial equations. Structured light reconstruction methods solve the problem of reconstruction failure in stereo vision methods due to a lack of features, making them more widely applicable. Additionally, structured light reconstruction methods are known for their simplicity, high reconstruction accuracy, and ease of implementation. However, they require the surface being reconstructed to have a certain degree of diffuse reflection. Surfaces that are mirror-like, transparent, or absorptive pose significant challenges for reconstruction.

Structured light comes in various types, distinguished by the shape of the projected patterns and the type of light source. Based on the projection pattern, structured light can be categorized into point structured light, line structured light, and grating structured light. Based on the light source, it can be divided into line structured light and projector structured light.

1) Point Structured Light: This type of structured light uses a point laser to project onto the target surface. The camera captures the reflected point image, and reconstruction is achieved using spatial triangulation. However, it can only obtain a limited number of points at a time, leading to low reconstruction efficiency [35–37].

2) Line Structured Light: Line structured light is generated using a scattering mirror group to produce line patterns. Each captured image can provide the depth of points along one or more lines. By translating the lines, the depth of a surface can be obtained. Line structured light offers higher reconstruction efficiency and is commonly used in current reconstruction devices [27, 38, 39].

3) Pseudo-random Speckle: This method uses the diffuse reflection of laser light on the target surface to produce highly random and distinctive speckle patterns. These patterns mark the space, and depth information is calculated based on geometric relationships for reconstruction [40–42].

Grating structured light is typically produced by projection devices. When reference fringes are projected onto the target surface, they deform according to the surface contours. A mathematical model of fringe deformation and surface shape is established based on system parameters. For 3D coordinate calculation, the sequence information of the projected fringes must be known. The process of assigning sequence information to the projected fringes is called encoding, while the process of solving the sequence information is called decoding. Common encoding rules include time encoding, spatial encoding, and direct encoding, with corresponding decoding methods varying based on the encoding approach.

In this paper, we choose line structured light as the method for validation. The proposed approach can be applied to point structured light or grating structured light as well.

## 2.2 Active Camera-projector 3D Reconstruction Systems

The 3D measurement of moving objects has garnered significant interest in various fields, such as industrial production inspection, robotic navigation, motion analysis, medical robotics, and virtual reality. Recognizing this need, scholars have explored various active sensing and 3D reconstruction methods for moving objects based on camera-projector systems [80].

One prominent approach is phase shifting profilometry, which has been developed to achieve high-accuracy reconstruction. However, these methods often face challenges in synchronizing the projection pattern with the object's motion, and the fixed field of view (FOV) of both the camera and projector restricts the reconstruction range. These limitations make it difficult to accurately reconstruct high-speed moving objects [83] [84]. Maruyama *et al.* [85] utilized a high-speed projector to enhance pattern projection and capture, achieving the reconstruction of objects moving at speeds of 300-500 mm/s. However, due to limited reconstruction range, this method cannot handle higher speed objects and the accuracy is still constrained by the projector's frame rate. Namiki *et al.* [86] developed an active vision approach using a pan-tilt platform for the camera and projector, capable of reconstructing objects moving at 1000 mm/s; however, detailed accuracy assessments were not provided as the study only presented point clouds. Blais *et al.* [87] proposed a new acquisition method for 3D laser scanners of freely moving objects, but it can only estimate the object's pose and does not achieve complete 3D reconstruction. Salil *et al.* [88] presented a technique for obtaining a 3D point cloud of a moving object by applying motion correction for a laser scanner, but its application is limited to slowly moving objects.

In light of these challenges, our study aims to develop an advanced active 3D reconstruction system that combines dynamic laser scanning and a dynamic camera setup using multiple galvanometers. This approach seeks to overcome the limitations of fixed FOV and synchronization issues, enabling high-precision and wide-range 3D reconstruction of moving objects.

## 2.3 Calibration Methods

Existing camera-projector calibration methods can be divided into two categories. The first category involves capturing both the calibration chessboard and the projected chessboard in the same scene [43, 44]. These methods use the calibrated parameters of the camera to calculate the parameters of the projector, leading to the accumulation and amplification of calibration errors from the camera during the projector calibration process. To avoid projector calibration being affected by the calibration errors of the camera, some researchers proposed the “inverse camera” method. In this approach, fringe patterns are generated and projected onto the calibration target, and the pixel coordinates of the feature points on the image plane of the projector are determined. The camera is used only to enable the projector to ”capture” the calibration target. The precision of these methods depends on the accuracy of extracting and mapping the corresponding pixel coordinates of feature points on the image plane of the camera and the projector. For instance, phase-shifting patterns are directly projected onto a printed chessboard, and feature points are extracted by the camera and mapped to their pixel coordinates on the projector’s image plane [45]. Zhang et al. [46] implemented sub-pixel mapping between corresponding feature points on the image planes of the camera and the projector, based on the projection invariance of the cross ratio. With the advancement of machine learning and deep learning, some learning-based calibration methods have also emerged. Liu et al. [47] proposed a Bayesian network based on the Markov random field hypothesis, transforming the image intersection point matching problem between a camera and a projector into a maximum a posteriori estimation problem. Yuan et al. [48] designed an unsupervised image deblurring network to recover a sharp target image from a deteriorated one, enabling more accurate feature learning from multi-quality target datasets.

However, these methods are all designed for static camera-projector systems. In this study, we propose a novel active light-section 3D reconstruction system that combines dynamic laser and dynamic camera using multi-galvanometers. Our approach utilizes multiple galvanometers to synchronize laser scanning and the FOV switching of the camera, enabling high-precision and wide-range 3D reconstruction. Calibration is required to achieve this, including the system calibration of the galvanometer-based dynamic laser and camera, and their joint calibration.

For calibrating galvanometer-based dynamic laser systems, Eisert [73] introduced a geometric model and calibration procedure; however, the model was complicated, and its optimization was difficult, thus leading to low accuracy. Yu [74] designed a one-mirror galvanometer laser scanner. However, the calibration procedure was complex, and the objective function was difficult to optimize. Similarly, Yang [75] proposed a calibration method based on a precision linear stage. However, this approach relies on a precision instrument and lacks flexibility.

For calibrating galvanometer-based dynamic camera systems, Ying *et al.*, [89–91] introduced self-calibration methods, which were complex in theory and difficult to implement. Kumar [93] proposed a calibration method based on the look-up table (LUT) using simple linear parameters, which required complex pre-processing. Junejo *et al.*, [89, 90, 92, 93] proposed feature-based calibration methods, which were time-consuming and had low accuracy. Han [94] introduced a calibration method for galvanometer-based camera using an end-to-end single-hidden layer feed forward neural network model, but it was computationally intensive. Boi *et al.*, [87] [29] proposed manifold constrained

Gaussian process regression methods for galvanometer setup calibration, which relied on data-driven and complex calibration procedures. Hu [95] built a galvanometer mirror-based stereo vision measurement system and established a mirror reflection model, but it still lacked an accurate calibration method.

Existing calibration methods only focus on calibrating either dynamic lasers or dynamic cameras and still have some shortcomings, as mentioned above. To address these limitations, this study proposes a novel comprehensive calibration solution for the proposed system, encompassing the calibration of the dynamic camera, dynamic laser, active tracking, and their joint calibration.

# Chapter 3

# Concept

## 3.1 Active Vision and Projection-Based 3D Reconstruction Method

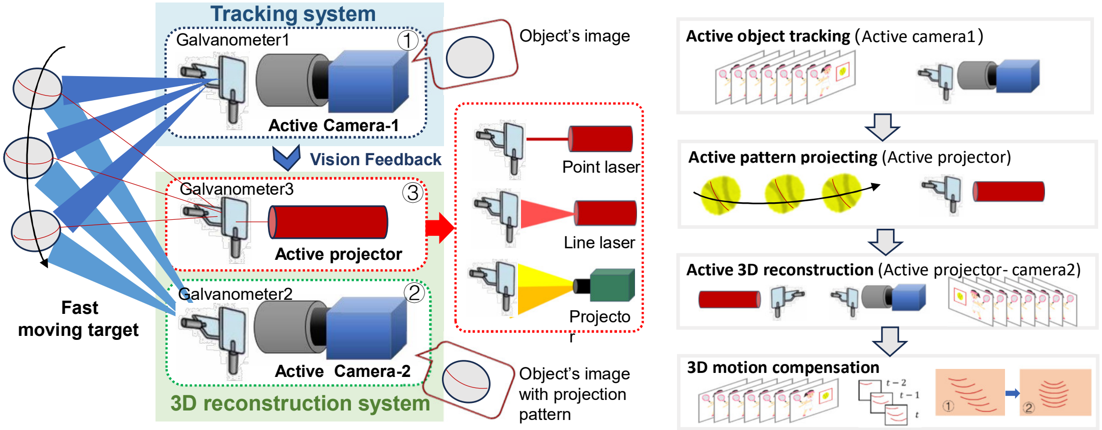

**Figure 3.1: Concept of active vision and projection-based 3D reconstruction.**

As analyzed in Chapter 1 and Chapter 2, existing Camera-Projector methods face significant challenges with 3D reconstruction of high-speed moving objects due to two primary reasons: the static nature of the system, with fixed cameras and projectors, which limits the 3D imaging range, and the lack of dynamic feedback on the target's motion, making it difficult to address reconstruction errors caused by the object's movement.

To address these challenges, this study proposes a High-Speed Active Camera-

Projector Based 3D Reconstruction Method for Moving Objects, conceptually depicted in Figure 3.1. The concept is to make the 3D reconstruction system dynamic through a galvanometer-based system, thereby expanding the reconstruction range. Furthermore, by introducing a tracking module, the moving target remains stationary relative to the 3D system.

The system comprises three main components: an active tracking camera system (labeled ①), an active reconstruction camera system (labeled ②), and an active projection system (labeled ③). System ① encompasses Galvanometer-1 and Camera-1, which work together to track the object. System ② includes Galvanometer-2 and Camera-2 for 3D reconstruction. System ③, consisting of Galvanometer-3 and a projection device, is responsible for projecting structured light onto the object. The projection light source in System ③ varies depending on the type of structured light reconstruction: it can be a point laser source for point structured light reconstruction, a line laser source for line structured light reconstruction, or a projector/planar light source for plane structured light reconstruction. These light sources are integrated into System ③ to enable different structured light reconstruction techniques, as necessitated by the specific application. In this paper, we choose the laser for validation using the light-section method.

## 3.2 Working Procedure

This system functions by first employing an active tracking camera (Camera-1) to monitor the motion of objects. Subsequent to this tracking, an active projection system projects patterns onto the objects based on the acquired tracking data. Concurrently, an active reconstruction camera (Camera-2) captures images of moving objects with these projection patterns, enabling 3D reconstruction. Before operating the system, a comprehensive calibration is essential. This includes calibrating Camera-1 and Galvanometer-1 to establish the relationship between the control voltage offset for Galvanometer-1 and

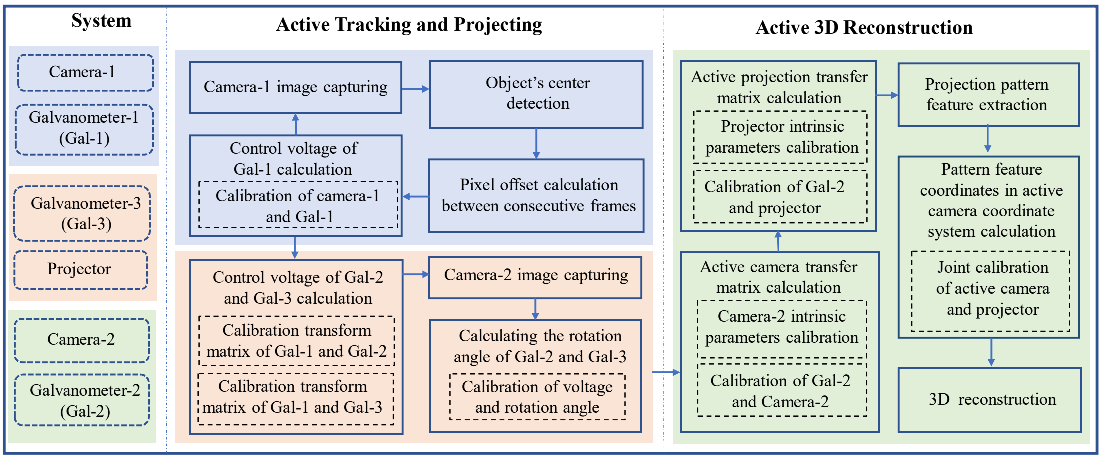

**Figure 3.2: Working procedure**

pixel offset for Camera-1; calibrating Galvanometer-1,2,3 to delineate the positional relationships among the galvanometers; and calibrating the relationship between the voltages of Galvanometer-2,3 and their rotational angles. Additionally, calibration of the intrinsic parameters of both Camera-2 and the projector is performed, along with calibration to determine the positional relationships between Camera-2 and Galvanometer-2, and between the projector and Galvanometer-3. A joint calibration of the active camera and active projector systems is also conducted. The specific calibration process is depicted in Figure 3.2, where solid frames indicate process steps and dashed frames highlight the calibration parameters required for each step.

Galvanometer-1 triggers Camera-1 to capture images. An object detection algorithm is employed to identify objects in the image and extract the center points of the objects. The pixel offset of the object center between consecutive frames is then calculated to adjust the control voltage of Galvanometer-1, ensuring the object remains centered in the image, thus achieving active tracking. Based on the control voltage of Galvanometer-1, the control voltage for Galvanometer-3 is calculated to project the pattern onto the object, achieving active projection. Similarly, the control voltage for Galvanometer-2 is computed, enabling Camera-2 to capture the object adorned with the projection pattern.

The rotational angles of Galvanometer-2 and Galvanometer-3 are calculated based on their control voltages, which then facilitates the computation of the transformation matrix of the active camera and active projector. Subsequently, feature extraction is performed on the images captured by Camera-2, and combined with the calibration results, the coordinates of the feature points within the active camera coordinate system are calculated to complete the 3D reconstruction and obtain the 3D point cloud of the moving object.

The entire research is divided into two parts. The first part is the development of an active 3D reconstruction system, where the galvanometer simultaneously drives the camera's field of view (FOV) and laser scanning. This dynamic system for both the camera and projection achieves large-range and high-precision 3D reconstruction, addressing the first issue of limited 3D reconstruction range for moving targets. The second part builds upon the first by adding a visual feedback system that tracks the target in real-time and feeds the target's movement information back to the active 3D reconstruction system. This resolves the second issue of synchronization between the moving target and the projection.

# Chapter 4

# A Novel Active Light-Section 3D Reconstruction Method for Wide-Range Sensing

## 4.1 Introduction

Light-section vision systems are widely used in many applications for their adaptability, high accuracy, and effective cost [56], such as rail traffic monitoring [49], medical imaging [58], robotics [51], and industrial production [31]. Such systems typically comprise a camera, laser projector, and mechanical scanning platform. The line laser projects laser stripes onto the surface of the object, whereas the camera captures an image of the object with the laser stripes. The three-dimensional (3D) geometric information of the object is then obtained by triangulation, as extensively reviewed in literature [57]. The 3D reconstruction of an object can be completed by passing laser stripes or objects through a mechanical scanning platform.

Traditional laser scanners rely primarily on mechanical driver shafts, which are large, complex, and slow [62], [58]. To overcome these limitations, various scanning mechanisms have been proposed. For instance, Du designed a system that mounts a line laser on the end of a robotic arm to improve scanning flexibility; however, its scanning accuracy was limited by the precision of the robotic arm. Jiang [67] proposed a system that uses gimbals to drive the laser and camera for scanning; however, the system size was significant, and its scanning speed was slow. In recent years, galvanometers have emerged as promising scanning devices because of their small size, fast rotation, and high control accuracy. This galvanometer-based solution provides a better alternative in terms of laser scanning accuracy and speed [72]. However, existing galvanometer-based laser-scanning systems are primarily designed to perform laser scanning while leaving the camera fixed. The limited FOV of a fixed camera causes a trade-off between the accuracy and the sensing range of the system, which significantly affects its efficiency.

In this study, we propose a novel dynamic light-section 3D reconstruction system that combines dynamic laser and dynamic camera using multi-galvanometers. Our approach utilizes multiple galvanometers to synchronize laser scanning and the FOV switching of the camera, thereby enabling high-precision and wide-range 3D reconstruction. Calibration is required to achieve this, which includes the system calibration of the galvanometer-based dynamic laser and camera, and their joint calibration. For calibrating galvanometer-based dynamic laser systems, Eisert [73] introduced a mathematical model and calibration procedure; however, the model was complicated, and its optimization was difficult, thus leading to low accuracy. Yu [74] designed a one-mirror galvanometer laser scanner. However, the calibration procedure was complex, and the objective function was difficult to optimize. Similarly, Yang [75] proposed a calibration method based on a precision linear stage. However, this approach relies on a precision instrument and lacks flexibility. For calibrating galvanometer-based dynamic camera systems, Ying *et al.*, [89–91] introduced self-calibration methods, which were complex in theory and difficult to implement. Kumar [93] proposed a calibration method based on the look-up table (LUT) using simple linear parameters, which required complex pre-processing. Junejo *et al.*, [89, 90, 92, 93] proposed feature-based calibration methods, which were time-consuming and had low accuracy. Han [94] introduced a calibration method for galvanometer-based camera using an end-to-end single-hidden layer feed forward neural network model, but it was computationally intensive. Boi *et al.*, [87] [29] proposed manifold constrained Gaussian process regression methods for galvanometer setup calibration, which relied on data-driven and complex calibration procedures. Hu [95] built a galvanometer mirror-based stereo vision measurement system and established a mirror reflection model, but it still lacked an accurate calibration method.

In conclusion, current light-section 3D reconstruction systems cannot simultaneously have high accuracy and wide range. Moreover, existing calibration methods only focus on calibrating either dynamic lasers or dynamic cameras and still have some shortcomings, as mentioned above. To address these limitations, this study proposes a novel dynamic 3D reconstruction system that overcomes the trade-off between accuracy and measurement range by synchronizing laser scanning and FOV switching of a camera based on multiple galvanometers. Additionally, we propose a novel comprehensive calibration solution for the proposed system, encompassing the calibration of the dynamic camera, dynamic laser, and their joint calibration. The contributions of this study can be summarized as follows:

1) A novel dynamic light-section 3D reconstruction system is designed based on multiple galvanometers. To the best of our knowledge, the system is the first to synchronize laser scanning and FOV switching of camera, thus enabling high-precision and wide-range 3D reconstruction simultaneously.

2) A novel high-precision and flexible calibration method for the dynamic 3D system is proposed by constructing an error model and objective function based on the combined model of the dynamic camera and dynamic laser. This method is not only applicable to the proposed system but also to other single galvanometer-based dynamic laser or camera systems.

3) Experiments are conducted to validate the proposed dynamic 3D reconstruction method and demonstrate its accuracy. To the best of our knowledge, compared to all existing

galvanometer-based laser scanning methods, our approach has the highest measurement range while maintaining the same level of measurement accuracy.

## 4.2 System Design

The dynamic light-section 3D reconstruction system consists of a CMOS camera, a line laser, and two galvanometer mirror systems, as shown in Fig. 4.1. The camera and Galvanometer-1 form a dynamic camera system, whereas the laser and Galvanometer-2 form a dynamic laser system.

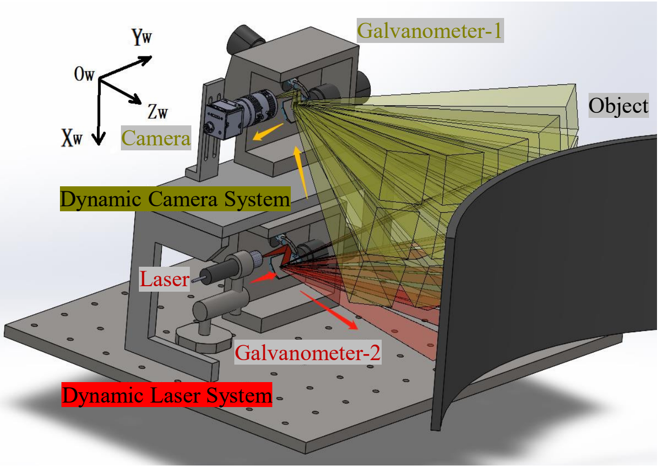

**Figure 4.1: System design.**

Based on the geometric model of the system and pre-calibration, the 3D information of the target can be calculated from the captured laser image and voltage values of the two galvanometers. The working principle is illustrated in Fig. 5.1. A spherical object on a flat plane is employed to demonstrate the process of dynamic 3D reconstruction. First, the system utilizes multi-galvanometer control to scan the target surface. When the system is activated, a line laser projects a laser stripe onto Galvanometer-2, which reflects the stripe onto the surface of the object. By controlling the voltage of Galvanometer-2, the laser stripe can scan the target. Simultaneously, the dynamic camera system captures

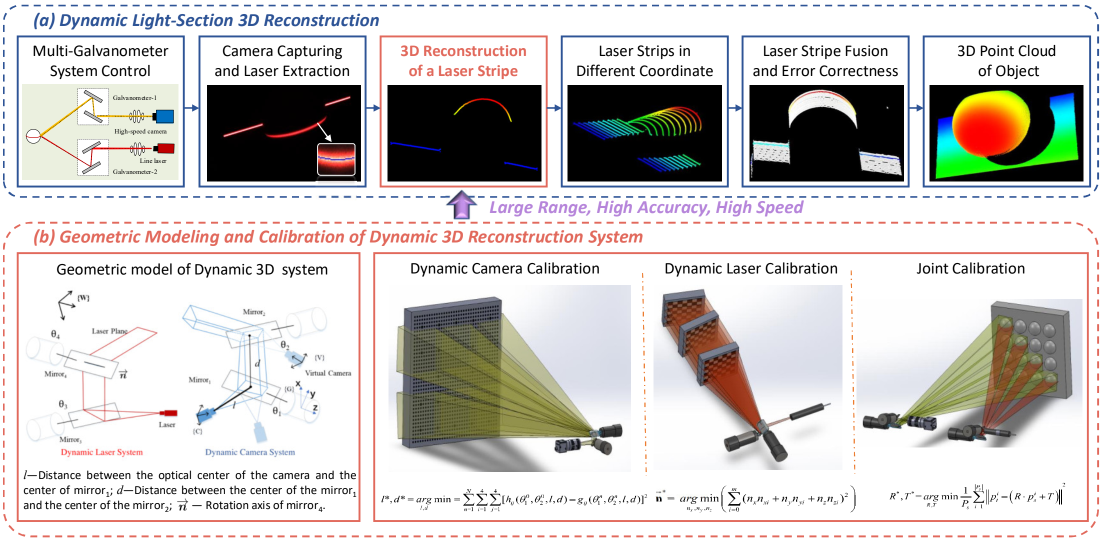

**Figure 4.2: Framework of dynamic 3D reconstruction method. (a) The flowchart of dynamic light-section 3D reconstruction. (b) Geometric modeling and calibration of dynamic 3D reconstruction system.**

laser images from different angles by adjusting the voltage of Galvanometer-1. Next, the laser-center-pixel coordinates are obtained using the laser stripe extraction algorithm. The 3D reconstruction of the laser stripe is performed by combining the voltage values of multiple galvanometers, laser pixel coordinates, geometric models of the dynamic 3D reconstruction system, and calibrated parameters. The point clouds of all the laser stripes are converted to the same coordinate frame using the transformation matrix of the dynamic camera. The system performs error correction based on the joint calibration to optimize accuracy. Finally, the system generates a point cloud for the target and completes the dynamic 3D reconstruction. Accurate geometric modeling and calibration methods are essential to ensure the 3D reconstruction accuracy of the system.

## 4.3 Geometric Model

The geometric model of the system is shown in Fig. 5.1(b). When the system is precisely machined, we can assume that for the dynamic camera system, the optical axis of the camera is perpendicular to the rotation axis of Galvanometer-1's pan mirror and incident at the center of the pan mirror. For the dynamic laser system, the laser plane is perpendicular to the rotation axis of Galvanometer-2's pan mirror and incident on the center of the mirror. Four coordinate frames are established. $\{W\}$ is the world coordinate frame, defined on the surface of the planar chessboard target, with the origin point O located at the upper-left corner of the chessboard. The X-axis and Y-axis are parallel to the chessboard array, while the Z-axis is perpendicular to the O-XY plane, following to the right-hand coordinate system. $\{C\}$ represents the camera coordinate frame, where the Z-axis corresponds to the camera's optical axis, and the X- axis and Y- axis are parallel to the image plane, following the right-hand coordinate frame. $\{G\}$ denotes the coordinate frame of Galvanometers-1, with the Z-axis corresponding to the rotation axis of the pan mirror. The X-axis is aligned with the camera's optical axis, while the Y-axis aligns with the line connecting the center points of the pan and tilt mirrors. $\{V_t\}$ is the virtual camera coordinate frame, formed by the reflection of $\{C\}$ through the pan and tilt mirrors of Galvanometers-1. According to the operating principle of a galvanometer, the rotation angle of the pan-tilt mirror is proportional to the voltage. For Galvanometer-1, the voltages of the pan-tilt mirrors are denoted by $U_{1-pan}$ and $U_{1-tilt}$. Therefore, the rotation angle of the pan mirror is $\theta_1 = k_{1-pan}U_{1-pan}$ and the rotation angle of the tilt mirror is $\theta_2 = k_{1-tilt}U_{1-tilt}$. As the pan-tilt mirror rotates, $\{V_t\}$ reflects the change in $U_{1-pan}$ and $U_{1-tilt}$. When $U_{1-pan} = U_{1-tilt} = 0$, the initail virtual camera coordinate frame is denoted by $\{V_0\}$. The relationship between $\{V_t\}$ and $\{V_0\}$ is given by Eq. (5.1).

$$^{V_t}\boldsymbol{T}_{V_0} = {}^{V_t}\boldsymbol{T}_G {}^G\boldsymbol{T}_{V_0}, \tag{4.1}$$

where $^{V_t}\boldsymbol{T}_{V_0}$ is the transformation matrix between $\{V_0\}$ and $\{V_t\}$. $^{V_t}\boldsymbol{T}_G$ denotes the transformation matrix between $\{G\}$ and $\{V_t\}$. $^G\boldsymbol{T}_{V_0}$ denotes the transformation matrix between $\{V_0\}$ and $\{G\}$. As shown in the geometric model diagram, $\{C\}$ is first reflected by

$$
{}^{V_t}\boldsymbol{T}_G = \begin{bmatrix} 1 & 0 & 0 & 0 \\ 0 & \cos 2\theta_2 & \sin 2\theta_2 & d(1-\cos 2\theta_2) \\ 0 & \sin 2\theta_2 & -\cos 2\theta_2 & -d\sin 2\theta_2 \\ 0 & 0 & 0 & 1 \end{bmatrix} \begin{bmatrix} -\cos 2\theta_1 & \sin 2\theta_1 & 0 & 0 \\ \sin 2\theta_1 & \cos 2\theta_1 & 0 & 0 \\ 0 & 0 & 1 & 0 \\ 0 & 0 & 0 & 1 \end{bmatrix} \begin{bmatrix} 0 & 0 & 1 & -l \\ 1 & 0 & 0 & 0 \\ 0 & 1 & 0 & 0 \\ 0 & 0 & 0 & 1 \end{bmatrix} =
$$

$$
\begin{bmatrix} \sin 2\theta_1 & 0 & -\cos 2\theta_1 & l\cos 2\theta_1 \\ \cos 2\theta_1 \cos 2\theta_2 & \sin 2\theta_2 & \sin 2\theta_1 \sin 2\theta_2 & -l\sin 2\theta_1 \cos 2\theta_2 + d(1-\cos 2\theta_2) \\ \cos 2\theta_1 \sin 2\theta_2 & -\cos 2\theta_2 & \sin 2\theta_1 \sin 2\theta_2 & -l\sin 2\theta_1 \sin 2\theta_2 - d\sin 2\theta_2 \\ 0 & 0 & 0 & 1 \end{bmatrix}. \tag{4.3}
$$

a pan mirror and then by a tilt mirror. The geometries of the two reflections are modeled using Eq. (5.2). For $\{V_0\}$, the rotation angle of the pan-tilt mirror is $\theta_1 = \theta_2 = 45°$. The transformation matrix ${}^{V_t}\boldsymbol{T}_{V_0}$ is calculated using Eq. (5.3). Thus, the geometric model of the dynamic camera is established.

$$
{}^{V_t}\boldsymbol{T}_{V_0} = {}^{V_t}\boldsymbol{T}_G {}^{V_0}\boldsymbol{T}_G^{-1} |(U_{1-pan} = U_{1-tilt} = 0). \tag{4.2}
$$

The coordinates of the pixel points on the laser stripe are denoted by $(u, v)$. The coordinates of the corresponding 3D points in $\{V_t\}$ are denoted by $(X_V, Y_V, Z_V)$. Based on the pinhole model of the camera, the mapping relationship between their coordinates can be obtained using Eq. (5.5).

$$
Z_V \begin{bmatrix} u \\ v \\ 1 \end{bmatrix} = \begin{bmatrix} f_x & 0 & u_0 \\ 0 & f_y & v_0 \\ 0 & 0 & 1 \end{bmatrix} \begin{bmatrix} X_V \\ Y_V \\ Z_V \end{bmatrix}, \tag{4.4}
$$

where $(u_0, v_0)$ is the principal point of the image, $f_x$ and $f_y$ are the focal length of the camera. For Galvanometer-2, the rotation angle of the pan mirror is denoted by $\theta_3 =$

$k_{2-pan}U_{2-pan}$, and the rotation angle of the tilt mirror is denoted by $\theta_4 = k_{2-tilt}U_{2-tilt}$. When $U_{2-pan} = U_{2-tilt} = 0$, the dynamic laser is in its initial position. The initial laser plane in $\{V_0\}$ is denoted by ${}^{V_0}plane_0$ and its equation is $A_0x + B_0y + C_0z + D_0 = 0$. The rotation axis of the dynamic laser in $\{V_0\}$ is denoted as $\overrightarrow{\boldsymbol{n}} = (n_x, n_y, n_z)$. The plane of the laser after rotation about the rotation axis is denoted as ${}^{V_0}plane$, and the equation is $A_{V_0}x + B_{V_0}y + C_{V_0}z + D_{V_0} = 0$.

The light path of the dynamic laser is reflected by a mirror and rotated along its axis. The rotation angle of the laser plane is twice that of the mirror plane. Therefore, the equation for the dynamic laser plane after rotation in $\{V_0\}$ can be solved using Eq. (5.6),

$$\begin{bmatrix} A_{V_0} \\ B_{V_0} \\ C_{V_0} \end{bmatrix} = \boldsymbol{R}\left(\overrightarrow{\mathbf{n}}, 2\theta_4\right) \begin{bmatrix} A_0 \\ B_0 \\ C_0 \end{bmatrix}, \tag{4.5}$$

where $\boldsymbol{R}$ represents the Rodrigues transformation. Using a point $\boldsymbol{P} = (X_0, Y_0, Z_0)$ on the rotation axis, $D_{V_0}$ can be calculated as $D_{V0} = -A_{V_0}X_0 - B_{V_0}Y_0 - C_{V_0}Z_0$. Combining this with the transformation matrix ${}^{V_t}\boldsymbol{T}_{V0}$ in Eq. (5.3), the equation for the dynamic laser plane in $\{V_t\}$ can be calculated as

$${}^{V_t}plane = {}^{V_t}\boldsymbol{T}_{V_0}{}^{V_0}plane. \tag{4.6}$$

The equation for ${}^{V_t}plane$ is denoted as $A_Vx + B_Vy + C_Vz + D_V = 0$. By extracting the pixel points $(u, v)$ from the laser stripe, the corresponding 3D point can be calculated as ${}^{V_t}\boldsymbol{P} = (X_V, Y_V, Z_V)$. Therefore, the relationship between ${}^{V_t}\boldsymbol{P}$ and the change in the galvanometer mirror angles can be expressed by Eq. (5.8).

$$\begin{cases} Z_V = D_V/[A_V \times (u - u_0)/f_x + B_V \times (v - v_0)/f_y + C_V] \\ X_V = (u - u_0)/f_x \times Z_V \\ Y_V = (v - v_0)/f_y \times Z_V \\ \{A_V, B_V, C_V, D_V\} = \boldsymbol{F}\left(\theta_1, \theta_2, \theta_4; A_0, B_0, C_0, D_0, l, d, \overrightarrow{\mathbf{n}}, \mathbf{P}\right). \end{cases} \tag{4.7}$$

$\boldsymbol{F}$ represents a parameterized mapping function, where $\theta_1, \theta_2, \theta_4$ are variables and other parameters are constants. Because $\{V_t\}$ changes constantly with the scanning angle, it is necessary to convert all ${}^{V_t}\boldsymbol{P}$ into a coordinate frame that is fixed with $\{W\}$. For ease of calculation, we choose $\{V_0\}$ and obtain ${}^{V_0}\boldsymbol{P} = (X_{V_0}, Y_{V_0}, Z_{V_0}) = {}^{V_0}\boldsymbol{T}_{V_t}{}^{V_t}\boldsymbol{P}$.

Thus, we establish the relationship between $(u, v)$ and $(X_{V_0}, Y_{V_0}, Z_{V_0})$ to formulate the 3D reconstruction. In the geometric model of the 3D dynamic system, Eq. (5.8) shows that $f_x, f_y, u_0, v_0$ can be obtained by calibrating the camera. $A_0, B_0, C_0, D_0$ can be obtained from the laser plane calibration. $l, d, \overrightarrow{\boldsymbol{n}} = (n_x, n_y, n_z), \boldsymbol{P} = (X_0, Y_0, Z_0)$ are unknown, and a calibration algorithm must be designed to obtain the unknowns.

## 4.4 Calibration Method

The proposed system calibration method is divided into three parts: the dynamic camera calibration, the dynamic laser calibration, and the joint calibration of the dynamic camera and laser for error correction.

### 4.4.1 Dynamic Camera Calibration

To calibrate the intrinsic parameters, $f_x, f_y, u_0, v_0$, of the camera, we use the method proposed by Zhang. The dynamic camera mathematical model described in Section II is used to determine the constraint relationship between $\{V_i\}$ and $\{G\}$, as shown in Eq. (5.2); thus, we can obtain the parameters $l$ and $d$. The proposed dynamic camera calibration method uses a large calibration board as shown in Fig. 5.1(b). The calibration board measures 740 × 740 mm and comprises a total of 35 × 35 circular markers. These markers are constructed from 25 individual 7 × 7 sub-patterns. Each sub-pattern features a central larger circular marker with a diameter of 15 mm, while the remaining smaller circular markers have a diameter of 10 mm, with a center-to-center spacing of 20 mm. The purpose of the larger circular markers is to establish the relationships between calibration points across different FOVs. The calibration board is scanned by varying the galvanometer voltage to obtain numerous images at different rotation angles. Each image corresponds to a virtual coordinate frame. The number of images is denoted as $n$. The transformation matrix between $\{V_i\}$ and $\{W\}$ is obtained through Zhang's extrinsic parameter calibration method, denoted as ${}^{V_0}\boldsymbol{T}_W, {}^{V_1}\boldsymbol{T}_W, {}^{V_2}\boldsymbol{T}_W, \ldots, {}^{V_n}\boldsymbol{T}_W$. As the relative positions between the calibration points in these images are known, the transformation matrix between virtual coordinate frames is calculated as ${}^{V_1}\boldsymbol{T}_{V_0}, {}^{V_2}\boldsymbol{T}_{V_0}, \ldots, {}^{V_n}\boldsymbol{T}_{V_0}$. These values are taken as observations. Multiple sets of observations are used to solve for the parameters to be calibrated. The initial pan-tilt angles of Galvanometer-1 are denoted by $\theta_1^{(0)}$ and $\theta_2^{(0)}$. They are the corresponding angles of $\{V_0\}$ and the first calibration image. The pan-tilt angles of Galvanometer-1 corresponding to $\{V_n\}$ and $n$th calibration images are denoted as $\theta_1^{(n)}$ and $\theta_2^{(n)}$. Therefore, $\{V_0\}$ and $\{V_n\}$ are defined as follows:

$$\begin{aligned} {}^{V_0}\boldsymbol{T}_G &= {}^{V_i}\boldsymbol{T}_G|_{\theta_1=\theta_1^{(0)},\theta_2=\theta_2^{(0)}} = k_{ij}(\theta_1^{(0)},\theta_2^{(0)},l,d), \\ {}^{V_n}\boldsymbol{T}_G &= {}^{V_i}\boldsymbol{T}_G|_{\theta_1=\theta_1^{(n)},\theta_2=\theta_2^{(n)}} = g_{ij}(\theta_1^{(n)},\theta_2^{(n)},l,d), \end{aligned} \tag{4.8}$$

where $k_{ij}$ and $g_{ij}$ represent the function of ${}^{V_0}\boldsymbol{T}_G$ and ${}^{V_n}\boldsymbol{T}_G$. $l$ and $d$ are parameters to be calibrated using Eq. (5.8). The transformation matrix between $\{V_0\}$ and $\{V_n\}$ is a 4×4 matrix, which can be expressed as:

$$
{}^{V_n}\mathbf{T}_{V_0}(n) = \begin{bmatrix} a_{11}^n & a_{12}^n & a_{13}^n & a_{14}^n \\ a_{21}^n & a_{22}^n & a_{23}^n & a_{24}^n \\ a_{31}^n & a_{32}^n & a_{33}^n & a_{34}^n \\ 0 & 0 & 0 & 1 \end{bmatrix} = a_{ij}^n. \tag{4.9}
$$

Simultaneously, ${}^{V_n}\boldsymbol{T}_G$ can be calculated using ${}^{V_0}\boldsymbol{T}_G$ from Eq. (4.8), and ${}^{V_n}\boldsymbol{T}_{V_0}$. For ease of representation, this is denoted as $h_{ij}$.

$$
\begin{aligned} &{}^{V_n}\boldsymbol{T}_G = {}^{V_n}\boldsymbol{T}_{V_0}(n) \cdot {}^{V_0}\boldsymbol{T}_G = \\ &\sum_{i=1}^{4}\sum_{j=1}^{4} a_{ij}^n k_{ij}\left(\theta_1^{(0)}, \theta_2^{(0)}, l, d\right) = h_{ij}\left(a_{ij}^n, \theta_1^{(0)}, \theta_2^{(0)}, l, d\right) \end{aligned} \tag{4.10}
$$

Eq. (5.11) is the result of $\{V_i\}$ obtained from multiple observations. Eq. (4.8) shows the results calculated using the mathematical model of the dynamic camera. For all the measured coordinate frames ($\{V_0\}, \{V_1\}, \{V_2\}, \ldots, \{V_n\}$), the sum of the errors between the theoretical and measured values must be minimized. Therefore, the objective function is formulated using Eq. (5.17).

$$
\begin{aligned} &l*, d* = \underset{l,d}{\arg\min} \sum_{n=1}^{n}\sum_{i=1}^{4}\sum_{j=1}^{4} \\ &\left[h_{ij}\left(a_{ij}^n, \theta_1^{(0)}, \theta_2^{(0)}, l, d\right) - g_{ij}\left(\theta_1^{(n)}, \theta_2^{(n)}, l, d\right)\right]^2. \end{aligned} \tag{4.11}
$$

In Eq. (5.2), the parameters $l$ and $d$ exist only in translation vector. Based on the objective function, Eq. (5.15) can be obtained. Finally, the parameters $l$ and $d$ are obtained by solving Eq. (5.15) using the least-square method.

$$\begin{cases} g_{14}\left(\theta_1^{(1)}, \theta_2^{(1)}, l, d\right) - h_{14}\left(a_{ij}^{1}, \theta_1^{(0)}, \theta_2^{(0)}, l, d\right) = 0 \\ g_{24}\left(\theta_1^{(1)}, \theta_2^{(1)}, l, d\right) - h_{24}\left(a_{ij}^{1}, \theta_1^{(0)}, \theta_2^{(0)}, l, d\right) = 0 \\ g_{34}\left(\theta_1^{(1)}, \theta_2^{(1)}, l, d\right) - h_{34}\left(a_{ij}^{1}, \theta_1^{(0)}, \theta_2^{(0)}, l, d\right) = 0 \\ \dots \\ g_{14}\left(\theta_1^{(n)}, \theta_2^{(n)}, l, d\right) - h_{14}\left(a_{ij}^{n}, \theta_1^{(0)}, \theta_2^{(0)}, l, d\right) = 0 \\ g_{24}\left(\theta_1^{(n)}, \theta_2^{(n)}, l, d\right) - h_{24}\left(a_{ij}^{n}, \theta_1^{(0)}, \theta_2^{(0)}, l, d\right) = 0 \\ g_{34}\left(\theta_1^{(n)}, \theta_2^{(n)}, l, d\right) - h_{34}\left(a_{ij}^{n}, \theta_1^{(0)}, \theta_2^{(0)}, l, d\right) = 0. \end{cases} \tag{4.12}$$

### 4.4.2 Dynamic Laser Calibration

Based on the mathematical modeling of the dynamic laser presented in Section II, the equation of ${}^{V_0}plane_0$ and the rotation axis of the dynamic laser $\vec{n}$ must be calibrated when Galvanometer-1 is at the initial position. The calibration of ${}^{V_0}plane_0$ is conducted utilizing the methodology outlined in [?]. This process involves the acquisition of laser images at various positions using a checkerboard calibration plate. Through this approach, the laser plane is accurately defined by fitting multiple laser lines. For the extraction of the laser center, the technique described in [32] is employed, offering the advantage of sub-pixel precision in the extraction process. Following these procedures, we successfully derive the equation $A_0x + B_0y + C_0z + D_0 = 0$.

The Galvanometer-2 voltage $U_{2-tilt} = U_1, U_2, \dots, U_m$ are used to move the laser and obtain multiple laser planes. Next, the respective equations are calibrated in the same manner as ${}^{V_0}plane_0$ and denoted as ${}^{V_0}plane_1, {}^{V_0}plane_2, \dots, {}^{V_0}plane_m$. The unit normal vectors of these planes are calculated as $\vec{n}_0(n_{x_0}, n_{y_0}, n_{z_0}), \vec{n}_1(n_{x_1}, n_{y_1}, n_{z_1}), \vec{n}_2(n_{x_2}, n_{y_2}, n_{z_2}), \dots, \vec{n}_m(n_{x_m}, n_{y_m}, n_{z_m})$. In the absence of errors, the laser planes intersect along the same straight line. This line is the laser rotation axis $\vec{n}$ and is also the rotation axis of the tilt mirror in Galvanometer-2. For a normal vector in any laser plane, we obtain $\vec{n} \cdot \vec{n}_i = 0 (i = 0, 1, 2, \dots, m)$. However,

$\vec{\boldsymbol{n}} \cdot \vec{\boldsymbol{n}}_i$ do not exactly equal zero because of various errors. Therefore, for all laser planes, the objective function is formulated as shown in Eq. (4.13).

$$\vec{\mathbf{n}}^* = \underset{n_x,n_y,n_z}{\arg\min}\left(\sum_{i=0}^{m}\left(n_x n_{x_i} + n_y n_{y_i} + n_z n_{z_i}\right)^2\right). \tag{4.13}$$

The direction vector $\vec{\boldsymbol{n}}$ of the rotation axis is obtained by minimizing the objective function. $\boldsymbol{P} = (X_0, Y_0, Z_0)$ is a point on the rotation axis in all laser planes and can be obtained using the least-square method. All parameters in Eq. (5.8) are obtained by calibrating the camera, laser plane, dynamic camera, and dynamic laser. Thus, we complete the calibration of the proposed dynamic 3D system.

### 4.4.3 Joint Calibration for Error Correction

For a well-calibrated dynamic light-section 3D reconstruction system, there are two sources of error, dynamic camera and dynamic laser, as listed in Table 5.2.

This study proposes an error correction method based on the joint calibration of a dynamic camera and dynamic laser. After the calibration is completed, error correction is performed based on the 3D reconstructed results. Theoretically, when Galvanometer-1 is scanning and Galvanometer-2 is fixed, the reconstructed laser point cloud coincides perfectly. However, as explained in the error source analysis, there is some deviation between the multiple laser point clouds owing to these errors. We correct these errors using point-cloud registration based on the Iterative Closest Point (ICP) algorithm [28] to obtain the accuracy transformation matrix.

The calibration process is designed based on the following principle. If Galvanometer-2 remains stationary, the laser will be out of the FOV after Galvanometer-1 has scanned a certain range. Therefore, multiple calibration positions must be set in advance to maintain the laser in the FOV. These are set in advance as $p_1, p_2, \ldots, p_n$ and the corresponding volt-

**Table 4.1: Error Source and Analysis**

| | Error | Source and Analysis |
|---|---|---|
| 1 | Rotation angle of galvanometer mirror ($\theta 1, \theta 2$) | Non-linear deviations exists between voltage and rotation angle of Galvanometer-1. |
| 2 | Dynamic camera geometric model | The spectacular reflection geometric model has deviations with mechanical structure. |
| 3 | Calibration of parameter ($l, d$) | This error has been optimized by proposed error model and objective function in this paper. |
| 4 | Camera intrinsic parameters calibration | This non-linear error is optimized using the Zhang's [**?**] calibration method. |
| 5 | Rotation angle of galvanometer mirror ($\theta 3, \theta 4$) | Non-linear deviations exists between voltage and rotation angle of Galvanometer-2. |
| 6 | Dynamic laser geometric model | This error depends on the accuracy of the laser mechanical installation. |
| 7 | Calibration of laser rotation axis | This error is optimized by the proposed objective function. |
| 8 | Laser center curve extraction | Center extraction algorithm is based on the Hessian Matrix and ensures a high extraction accuracy. |

ages of Galvanometer-2 at these positions are $(s_1, t_1), (s_2, t_2), \dots, (s_n, t_n)$, respectively. The laser plane equations $plane_{p_1}, plane_{p_2}, \dots, plane_{p_n}$ at these positions are calibrated using the laser plane calibration method described in Part B. The voltage of Galvanometer-1 is denoted by ($s'_1$, $t'_1$), ($s'_2$, $t'_2$), ...,($s'_m$, $t'_m$), respectively. The error-correction flow is presented in Algorithm 2.

**Algorithm 1** Joint Calibration for Error Correction

```
 1: Input: $f_x, f_y, u_0, v_0; l, d; A_1, B_1, C_1, D_1, \dots, A_n, B_n, C_n, D_n; (s_1, t_1), (s_2, t_2), \dots, (s_n, t_n)$.
 2: Output: ${}^{V_0}\boldsymbol{T}_{V_1}, {}^{V_0}\boldsymbol{T}_{V_2}, \dots, {}^{V_0}\boldsymbol{T}_{V_m}$.
 3: Initialize: $i \leftarrow 1$, $(s, t) \leftarrow (s_1, t_1)$, $(s', t') \leftarrow f(s, t)$, du $\leftarrow 0.1$, ${}^{V_1}plane \leftarrow plane_{p_1}$, $\boldsymbol{M} \leftarrow$ Unit matrix.
 4: Using Eq. (5.8) to obtain the laser point cloud ${}^{V_0}\boldsymbol{P}_1$.
 5: while $i < m$ do
 6:     Laser Image capture and center curve extraction;
 7:     ${}^{V_i}plane = g(s, t, s', t')$;
 8:     Using Eqs. (5.1)(5.2)(5.3) to calculate ${}^{V}\boldsymbol{T}_{V_i}$;
 9:     ${}^{V}plane \leftarrow {}^{V}\boldsymbol{T}_{V_i} {}^{V_i}plane$;
10:     Using Eq. (5.8) to obtain the point cloud ${}^{V_0}\boldsymbol{P}_i$.
11:     ${}^{V}\boldsymbol{T}_{V_i} \leftarrow$ Transformation matrix between ${}^{V_0}\boldsymbol{P}_1$ and ${}^{V_0}\boldsymbol{P}_i$;
12:     ${}^{V_0}\boldsymbol{T}_{V_i} \leftarrow \boldsymbol{M} {}^{V}\boldsymbol{T}_{V_i}$;
13:     if $i\%50 == 0$ then
14:         $(s, t) \leftarrow (s_{(i/50)}, t_{(i/50)})$, ${}^{V_i}plane \leftarrow {}^{V}plane$;
15:         Using Step. (8) – Step. (11) to obtain point cloud $\boldsymbol{P}$.
16:         $\boldsymbol{M} \leftarrow$ Transformation matrix between $\boldsymbol{P}$ and ${}^{V_0}\boldsymbol{P}_i$;
17:     end if
18:     $i \leftarrow i + 1$;
19:     $(s', t') \leftarrow (s' + du \times i\%200, t' + 1 \times int(i/200))$;
20: end while
```

## 4.5 Experiment

The proposed dynamic 3D reconstruction system is built as shown in Fig. 5.5. The camera model is MV-CA004-10UC, with a pixel size of 6.9 $\mu$m × 6.9 $\mu$m, resolution of 720 pixels × 540 pixels, and frame rate of 500 fps. The exposure time of the camera to capture the dark image of the laser is 500 $\mu$s. The laser model is LXL65050-16 and the laser wavelength is 650 nm. The models of both Galvanometer-1 and Galvanometer-2 are TSH8310. The galvanometer is used to scan a range of ±20° using a control voltage range from $-10V$ to $+10V$. The maximum scan frequency is 1 kHz, with an angular resolution of 0.0008, thus, the system has the potential for high accuracy and resolution.

### 4.5.1 Calibration Accuracy Verification

#### 4.5.1.1 Dynamic camera calibration accuracy

Twenty-five images of the calibration board are collected when $U_{1-pan} = U_{1-tilt} = 0$. The camera is calibrated using Zhang's [**?**] calibration method in OpenCV. After calibration, the intrinsic parameters are $f_x = 7801.38$, $f_y = 7798.24$, $u_0 = 359.51$, and $v_0 = 269.54$. The focal length is 53.83 mm. According to the calibration method for the dynamic cameras presented in Section III, the system parameters are solved as $l = 83.45$ mm and $d = 22.14$ mm. Based on these calibration results, the mathematical model proposed in Section II can be used to calculate the theoretical transformation matrix for the pan-tilt mirror of Galvanometer-1 at different angles.

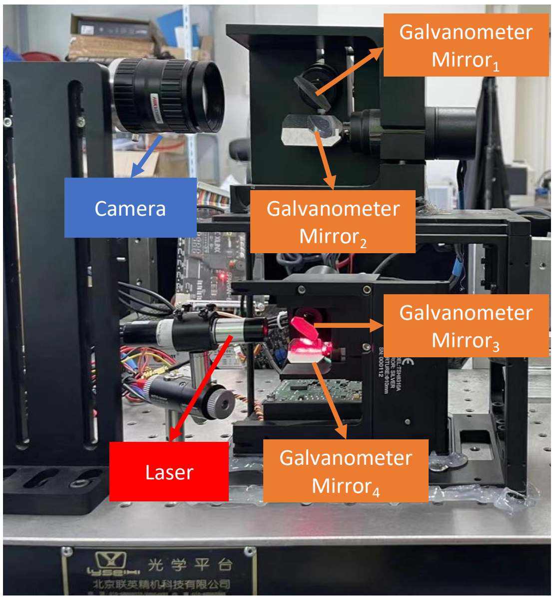

**Figure 4.3: 3D dynamic reconstruction system based on multiple galvanometers and light section.**

The transfer matrices corresponding to these angles are directly measured using a calibration board. The matrix 2-norm is calculated according to Eq. (4.14) to compare the theoretical matrices $\boldsymbol{A}$ and measured transfer matrices $\boldsymbol{B}$ for calibration accuracy verification. The pan-tilt voltages of Galvanometer-1 are varied from $-10V$ to $10V$, at intervals of $4V$. Thirty-six positions are measured. The error between the theoretical and measured transfer matrices is obtained, and the error curves are shown in Fig. 5.6(a). The results show that the RMSE (Root Mean Square Error) is 1.231 mm between the theoretical and measured values.

$$E(\boldsymbol{A},\boldsymbol{B}) = \sqrt{\sum_{i=1}^{4}\sum_{j=1}^{4}\left(\boldsymbol{A}_{ij} - \boldsymbol{B}_{ij}\right)^2} \tag{4.14}$$

This confirms the accuracy of the dynamic camera calibration. The observed errors originate from the geometric model and the calibration process, as explained in the error analysis section. It is important to note that the measured values obtained for the virtual camera using the calibration board may also exhibit slight deviations. Consequently, these findings serve as a validation of the accuracy of the dynamic camera calibration; however, these cannot be solely relied upon to assess the accuracy of the calibration. A more detailed accuracy verification can be conducted based on the outcomes of the 3D reconstruction analysis.

#### 4.5.1.2 Dynamic laser calibration accuracy

With Galvanometer-1 fixed, the calibration board is positioned within the FOV of the virtual camera. The tilt mirror of Galvanometer-2 is rotated 30 times with a step size of $0.1V$, allowing the system to scan the calibration board, whose position is randomly changed five times (ensuring clear imaging in the virtual camera); the same 30 scans are repeated for each position. The laser rotation axis is solved as $(\vec{\mathbf{n}}, \mathbf{P}) = ([0.99, 0.02, -0.0004], [-18310.30, -195.93, 257.97])$. Fig. 5.6(b) visually represents the laser plane and the rotation axis. Notably, the calibrated rotation axis align with the intersection of the laser planes, providing evidence for the accuracy of the dynamic laser calibration. A detailed accuracy assessment is subsequently performed by analyzing the results of the 3D reconstruction.

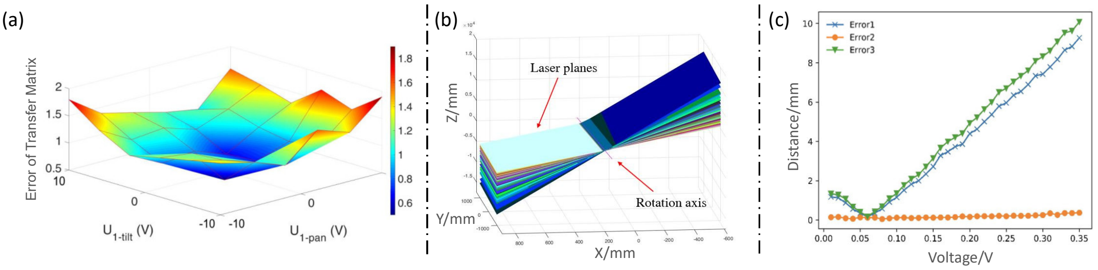

**Figure 4.4: Calibration accuracy verification. (a) Error of dynamic camera transformation matrix. (b) Visualization of laser planes and the calibrated rotation axis. (c) Error curve before and after correction.**

#### 4.5.1.3 Joint calibration accuracy

A calibration sphere is selected as the 3D reconstruction target for error correction. Galvanometer-2 is controlled to project the laser stripe onto the sphere, while Galvanometer-1 is fixed. The virtual camera, controlled by Galvanometer-1, captures images of the laser stripe from different views. The 3D reconstruction of these laser stripe images is performed based on the calibration results and mathematical models of the 3D dynamic system. The reconstructed point clouds, which are indicated as white, are shown in Fig. 5.1(a), 'Error Correction'. Notably, white point clouds exhibit non-overlapping regions owing to errors. The correction method described in Algorithm 2 is employed to register these white point clouds. The registration results are shown as colored point clouds in Fig. 5.1(a). The distance between the point clouds before and after the correction is calculated to evaluate the error. The calculation formula is as follows:

$$d = \frac{1}{|P_s|} \sum_{i=1}^{|P_s|} \left\| p_t^i - p_s^i \right\|^2, \tag{4.15}$$

here, $p_s$ represents the point cloud of the laser stripe captured in the first virtual camera view, and $p_t$ represents the point cloud of the laser stripe captured from another view. $|P_s|$ denotes the number of points in $p_s$. The error between $p_t$ and $p_s$ is determined by performing a nearest-neighbor search, denoted as Error1. After the point-cloud registration, the error between $p_t$ and $p_s$ is calculated as Error2. In addition, the error before correction is computed as Error3 using the matched points from the point-cloud registration result. The error curves are shown in Fig. 5.6(c). The RMSE of Error1 and Error3 before correction are calculated as 4.928 and 5.475 mm, respectively. However, after error correction, the RMSE of Error2 is significantly reduced to 0.197 mm. These results evidently indicate a substantial improvement in the accuracy following the error-correction process.

**Table 4.2: Accuracy and Reconstruction Range Comparison of Traditional and Proposed Methods.**

| Working distance/mm | Traditional methods | | | Proposed method | | |
|---|---|---|---|---|---|---|
| | Name Year | Accuracy/mm | Range/mm | Accuracy/mm | Range/mm | Factor of expanded range |
| 100 | NOM-LSS 2017 [16] | 0.01 | 10 × 10 | 0.01 | 130 × 200 | 260 |
| 250 | 3DM-LS 2018 [17] | 0.1 | 80 × 80 | 0.057 | 350 × 500 | 27.3 |
| | EAC-LSS 2020 [14] | 0.061 | 80 × 80 | | | |
| 350 | IS-LSS 2020 [30] | 0.08 | 200 × 200 | 0.08 | 500 × 700 | 8.75 |
| 400 | FFV-LSS 2007 [32] | 0.222 | 150 × 200 | 0.092 | 650 × 800 | 17.3 |
| | FLR-LSS 2022 [31] | 0.1 | 150 × 200 | | | |
| 1000 | U3D-LSS 2016 [33] | 0.382 | 200 × 300 | 0.314 | 1600 × 2000 | 53.3 |

### 4.5.2 3D Reconstruction Accuracy Verification

#### 4.5.2.1 Standard blocks reconstruction test

A standard stair block is employed to test the stability of the system and analyze its reconstruction accuracy at different angles. The stair block has a distance of 30 mm between its two planes, with machining errors within 1 $\mu$m. The 3D dynamic system proposed in the paper is used to reconstruct a stair block. Scanning is performed by synchronously controlling the tilt mirrors of both Galvanometer-1 and Galvanometer-2, rotating each by $0.1^\circ$. Once the scanning and reconstruction processes are completed, a point cloud of the stair block is generated. Two planes (Plane-1 and Plane-2) of the stairs are fitted, and the distance between them is calculated. Point clouds belonging to Plane-2 are used to fit a plane equation using the least-square method. Next, 500 points belonging to Plane-1 are randomly selected and the average distance between these points and Plane-2 is calculated as the distance of the fitted plane. The difference between the calculated and actual distances is considered as the error, which serves as a measure of the reconstruction accuracy achieved by the system.

The reconstruction distance is 650 mm. The FOV for a single virtual camera is 120 mm × 120 mm, while the dynamic camera's FOV expands to 1300 mm x 1300 mm (including a 10% overlap area for better stitching), thus enlarging the camera's imaging

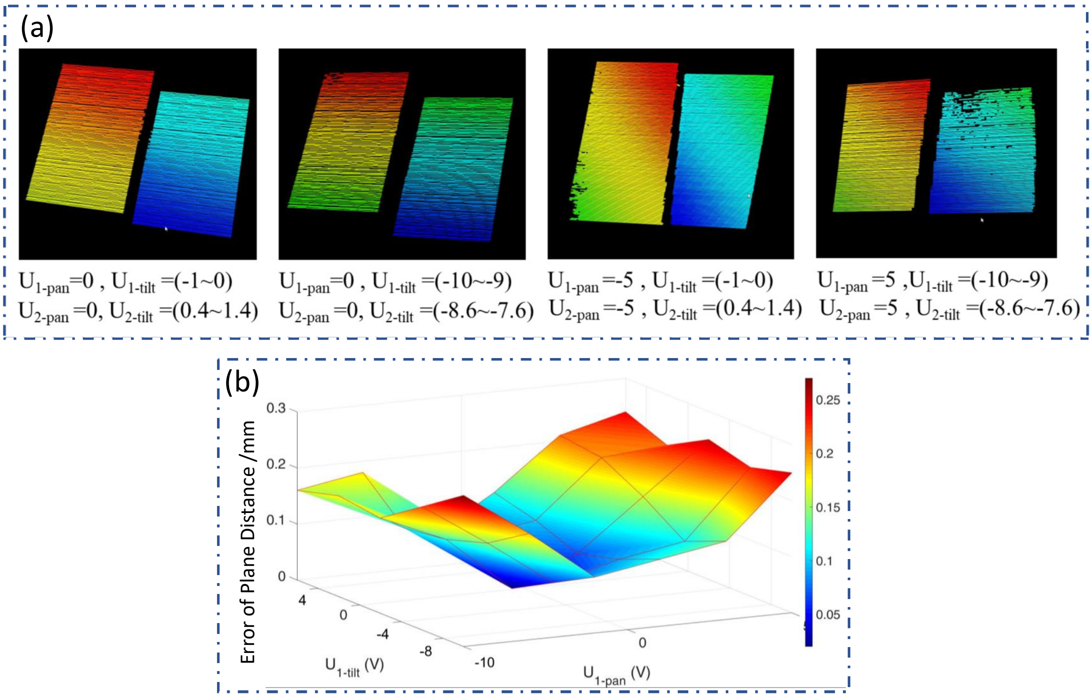

**Figure 4.5: Standard blocks reconstruction test at different angles. (a) The point clouds of the stair at different angle. (b) 3D reconstruction error distribution at different angles.**

range by a factor of 117.4. The scanning range of the dynamic laser is 1100 mm × 1640 mm. The measurement range of the system is determined by the overlapping FOV of the dynamic camera and dynamic laser, which measures 1100 mm × 1300 mm. Thirty different positions are selected to analyze the reconstruction accuracy at different angles. The dynamic camera and laser simultaneously scan the target from these positions to complete the 3D reconstruction process. Fig. 4.5(a) shows the example reconstructions obtained from four different positions, providing a visual representation of the reconstructed 3D models. The thickness error, which is related to the rotation angles of Galvanometer-1 and Galvanometer-2, is analyzed, as shown in Fig. 4.5(b). It is evident from the graph that the error in 3D reconstruction increases as the rotation angles of the galvanometers deviate from their initial positions (calibration position). This is because the camera's focal length is adapted to the calibration position, and imaging areas far from the calibration position may become blurred due to defocusing, thereby affecting accuracy. Furthermore, as analyzed in Table 5.2, errors due to various reasons accumulate more as the distance from the calibration position increases. The RMSE for these thirty positions is calculated as 0.165 mm. These values provide evidence of the high precision achieved by the proposed system for 3D reconstruction.

#### 4.5.2.2 Accuracy and reconstruction range comparison with existing methods

To compare the performance of the proposed method with that of existing methods [72, 74–78, 88], we conduct comparative experiments using the standard component scanning method. The accuracy of the dynamic light-section 3D system depends primarily on the working distance. To perform a fair comparison, we repeat the standard component scanning procedure at various reconstruction distances, namely 100, 200, 350, 400, and 1000 mm, which are consistent with the working distances employed in existing methods. As analyzed in the previous experiment, the system's reconstruction accuracy is related to the scanning position. In order to reduce errors other than calibration errors, we placed the target at the center of the scanning area.

The 3D reconstruction accuracy, measurement ranges of the traditional methods, and the magnification factor of the proposed method's reconstruction range compared to traditional methods are presented in Table 4.2. Fig. 4.6 more clearly shows the comparison of the reconstruction accuracy and range between traditional methods and our proposed method, with each color oval representing the same working distance. From the obtained results, it can be concluded that the proposed method exhibits smaller errors and larger measurement ranges than the existing methods at the corresponding working distances. This demonstrates the superior performance of our method in terms of accuracy and range compared with existing methods.

### 4.5.2.3 Large object scanning test

The high-precision machined large flat plate and sphere are also used to test the 3D reconstruction accuracy. The size of the plate is 740 mm × 740 mm, and the sphere has a diameter of 350 mm. Similar to the Experiment B (1), the system scans the target and obtains its point clouds with the scanning distance set at 650 mm, and the 3D measurement range is 1100 mm × 1300 mm. The position and angle of the target are arbitrarily changed within the scanning range, and the reconstruction is repeated three times for each target. For the plate target's point cloud, a plane equation is fitted using the RANSAC algorithm. The distances between all the points and the fitted plane are calculated, and the average of these distances is considered the error of the dynamic 3D system reconstruction. For the sphere target's point cloud, a sphere is fitted based on RANSAC algorithm, and the diameter is calculated. The difference between the calculated diameter and the sphere's actual diameter is taken as the error of the dynamic 3D reconstruction. The RMSE values for the three measurements are 0.281 mm for the plate and 0.226 mm for the sphere, respectively.

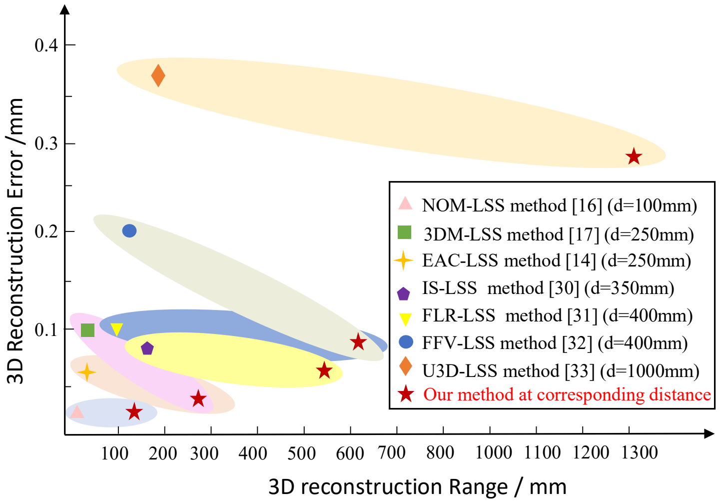

**Figure 4.6: Comparison of 3D reconstruction accuracy and measurement ranges between existing method and proposed method.**

This experimental result demonstrates that the system achieves sub-millimeter reconstruction accuracy within a meter-scale reconstruction range, indicating that the system enables high-precision multi-scale 3D reconstruction across a wide-range reconstruction area.

## 4.6 Concluding Remarks

A dynamic light-section 3D reconstruction system is proposed in this study, which overcomes the trade-off between accuracy and measurement range by using multiple galvanometers. A mathematical model of the system is established, and a flexible and accurate calibration method is developed. The experimental results demonstrate that the proposed system performs well in terms of measurements, indicating its potential for industrial applications where high-precision and wide-range 3D reconstruction is required. Furthermore, the proposed method can be used in conjunction with the active tracking system for 3D reconstruction of moving targets. This will be introduced in our other work.

# Chapter 5

# A Visual-Feedback Based Active Light-Section 3D Reconstruction Method for Moving Objects

## 5.1 Introduction

Light-section vision systems are widely applied fields such as rail traffic monitoring [49], medical imaging [50], robotics [51], and industrial production [52, 53] due to their adaptability, high accuracy, and cost-effectiveness [54–56]. Generally, these systems comprise a camera, laser projector, and mechanical scanning platform. The laser projector casts laser stripes onto the object's surface, which are then captured by the camera. The object's three-dimensional geometric information is subsequently obtained through triangulation, a process extensively reviewed in literature [57]. By manipulating the movement of either the laser stripes or the object through a mechanical scanning platform, 3D reconstruction of the object can be completed.

However, traditional laser scanning systems rely on mechanical driveshafts that are bulky, complex, and slow [58–61]. To enhance the scanning efficiency, a system with a line laser mounted on the end of a robotic arm was designed [62–66]. Despite improving the scanning flexibility, its accuracy was limited by the precision of the robotic arm. A gimbal-based system was proposed to drive the laser and camera for scanning [67–70], but the system was bulky, and the scanning speed was slow. The galvanometer has emerged as a promising scanning mechanism due to its compact size, fast rotation, and high control accuracy, ofafering a superior alternative to laser scanning and is widely used in various industrial inspection scenarios [71–79]. Despite these developments, existing systems lack feedback functionality, limiting their 3D reconstruction capabilities only to static objects.

The ability to achieve 3D reconstruction of moving objects is crucial for applications such as online industrial production inspection [28], robotic arm grasping for moving object navigation [29], motion analysis [30], high-precision positioning in medical robotics [31], and dynamic 3D data acquisition for virtual reality [32]. Recognizing this need, scholars have explored various active sensing and 3D reconstruction methods for moving objects [80]. 3D reconstruction methods for moving objects can be categorized into Time of Flight (TOF), Stereo Vision, and Camera-Projector techniques [81] [82]. Among these methods, the Camera-Projector technique is noted for its superior accuracy in reconstructing moving objects. Some researchers have developed high-accuracy reconstruction techniques based on phase shifting profilometry, however, these approaches often face challenges with synchronizing the projection pattern with the object's motion, and the fixed field of view (FOV) of both the camera and projector restricts the reconstruction range. These limitations make it challenging to accurately reconstruction high-speed moving objects [83] [84]. Maruyama *et al.* [85] utilized a high-speed projector to enhance pattern projection and capture, achieving the reconstruction of objects moving at speeds of 300-500 mm/s. However, due to limited reconstruction range, this method cannot handle higher speed objects and the accuracy is still constrained by the projector's frame rate. Namiki *et al.* [86] developed an active vision approach using a pan-tilt platform for the camera and projector, capable of reconstructing objects moving at 1000 mm/s; however, detailed accuracy assessments were not provided as the study only presented point clouds. Blais *et al.* [87] proposed a new acquisition method for 3D laser scanners of freely moving objects, but it can only estimate the object's pose and does not achieve complete 3D reconstruction. Salil *et al.* [88] presented a technique for obtaining a 3D point cloud of a moving object by applying motion correction for a laser scanner, but its application is limited to slowly moving objects.

In conclusion, on the one hand, existing light-section 3D reconstruction systems are not suitable for the reconstruction of moving objects due to the lack of visual feedback. On the other hand, the current methods for reconstructing moving objects still possess some shortcomings, as discussed above. To address this issue, this paper proposes a novel visual-feedback based active light-section 3D reconstruction method. This approach integrates a galvanometer-based tracking system with a dual-galvanometer-based active light-section 3D reconstruction system. Our strategy ensures synchronization between laser scanning, adjustment of the tracking camera's FOV, and modification of the 3D reconstruction camera's FOV, realized via the precise control of three galvanometers. This setup enables the tracking system to obtain the object's motion dynamics, and subsequently, sends this feedback to the active 3D reconstruction system. Consequently, the 3D vision system actively executes laser scanning and captures laser images to facilitate 3D reconstruction of moving objects. Additionally, we have devised a joint calibration technique for both the tracking and active 3D reconstruction systems, and introduced a 3D motion error compensation method. The contributions of this paper can be summarized as follows:

1) A novel active light-section 3D reconstruction system based on visual feedback is introduced. This system achieves the tracking and active 3D reconstruction of freely moving objects by synchronously controlling three galvanometer systems. To the best of our knowledge, this is the first system that utilizes the light-section technique to scan and reconstruct moving objects. It not only capitalizes on the high precision and robustness of the light-section technique but also overcomes its traditional limitations in scanning efficiency and adaptability to moving objects.

2) The geometrical model of the proposed system was developed by unifying the active tracking model, the active 3D reconstruction model, and the 3D motion error compensation model. Furthermore, an innovative and flexible calibration method was developed by formulating error models and corresponding objective functions. This enables the newly proposed system to achieve high-precision reconstruction of moving objects, attaining an accuracy level comparable to that of static object reconstruction.

The remainder of this article is organized as follows. The concepts underlying the work in this paper are introduced in Section II. In Section III, the proposed geometrical model is described in detail. Calibration methods are described in Section IV. Section V presents our validation experiments and results. Finally, Section VI concludes this article.

## 5.2 Framework

In laser scanning 3D reconstruction systems, the movement of the target can result in the laser scan not projecting at the anticipated location, thereby introducing errors into the 3D reconstruction results. To address this challenge, it is essential to employ visual feedback to ensure that the target remains stationary relative to the laser 3D reconstruction system, as conceptually depicted in Fig. 5.1(a). Initially, a visual system is required to track the target, capture the motion information, and feeding it back to the 3D reconstruction system. Subsequently, the laser 3D reconstruction system must also be dynamic, capable of real-time projection and capturing images of the target adorned with laser stripes based on the motion information. Due to the target's movement, there will be motion errors in relation to the world coordinates, although it remains stationary relative to the laser 3D reconstruction system. This necessitates 3D motion compensation to ultimately achieve 3D reconstruction of the moving target.

Consequently, the proposed visual feedback-based active light-section system is structured into three distinct subsystems. Subsystem-1 functions as the tracking mechanism, encompassing Galvanometer-1 and Camera-1. Both Subsystem-2 and Subsystem-3 collectively constitute the active 3D reconstruction mechanism. Subsystem-2, the dynamic camera system, integrates Galvanometer-2 and Camera-2. Subsystem-3, the dynamic laser system, comprises Galvanometer-3 and a laser module. The FOV for Camera-1 and Camera-2 can be modulated by manipulating Galvanometer-1 and Galvanometer-2, respectively. Similarly, the laser's projection position can be adjusted via Galvanometer-3. Through mathematical modeling, calibration, and image processing, this system enables the executing of the 3D reconstruction of moving objects.

The operational principle of the system is shown in Fig. 5.1(b). Galvanometer-1 triggers Camera-1 to capture Image-1 of the target. A target detection algorithm is applied to identify the target in Image-1 and calculate the pixel coordinates at the center. Based on the computed pixel coordinate ($\Delta$pixel) of the target's center between consecutive frames, the control voltage for Galvanometer-1 is determined to ensure that the target remains at the center of Image-1 and enables tracking. Based on the voltage of Galvanometer-1 and calibration parameters of Subsystem-1, the voltage for Galvanometer-2 is calculated, aligning the target with the center of Image-2 captured by Camera-2. Galvanometer-2 triggers Camera-2 to capture the laser image, and the center of the laser curve is extracted to obtain the pixel coordinates $(u, v)$ of the laser stripe.

Additionally, using the voltage of Galvanometer-1, calibration parameters of Subsystem-1 and Subsystem-3, and pixel coordinates of the target center, the control voltage for Galvanometer-3 is computed, enabling the laser stripe to scan the target. Furthermore, based on the calibration parameters of Subsystem-2 and Subsystem-3, as well as the rotation angles of Galvanometer-2 and Galvanometer-3, the rotation matrix for the dynamic camera and plane equation for the dynamic laser can be calculated. Consequently, the laser plane calculation in the dynamic camera coordinate system, denoted as ${}^{V}Plane$, is obtained. The combination of ${}^{V}Plane$ and $(u, v)$ enables the 3D reconstruction of the laser stripe. The reconstructed laser stripes are then fused into the same coordinate system for error correction. By using the calibration parameters of Subsystem-1 and Subsystem-2 and the voltage of Galvanometer-1, 3D motion error compensation for the target is performed. Finally, a complete 3D point cloud of the moving target is obtained. Throughout the entire process, accurate mathematical modeling and calibration of the system are crucial.

***(a) Concept of visual-feedback based active light-section 3D reconstruction***

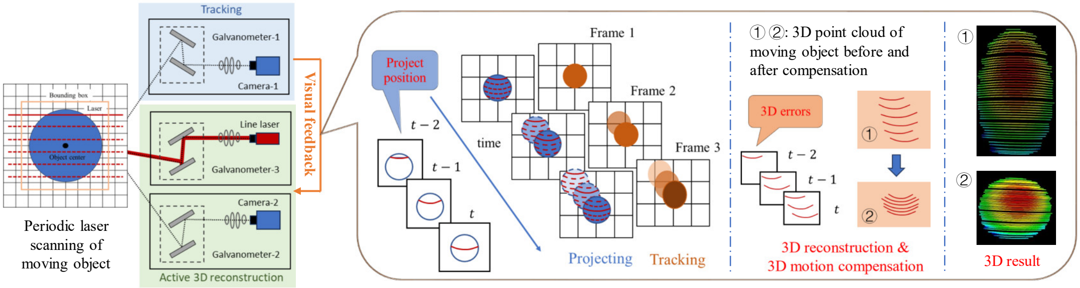

***(b) Working Principle***

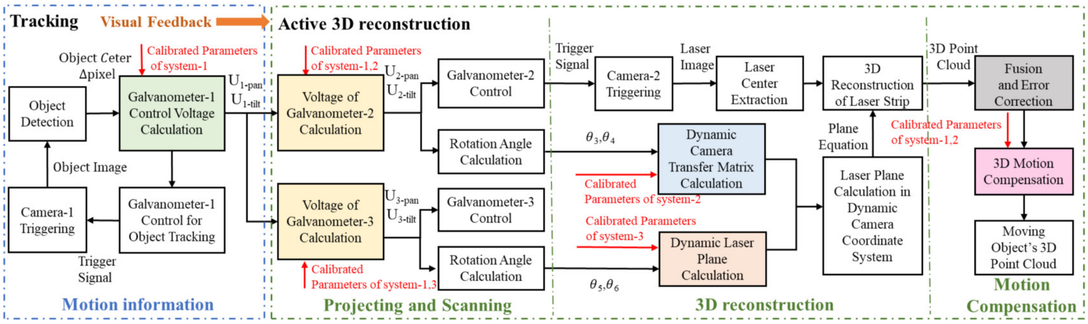

**Figure 5.1: Framework (a) Concept of visual-feedback based active light-section 3D reconstruction. (b) Working principle.**

## 5.3 System Design and Synchronization Strategy

The proposed system is shown in Figure. 5.2 and As illustrated in Figure. 5.3, the system's complex control sequence is segmented into four distinct components. Sequence ① governs Galvanometer-1, which is linked to the tracking function of Camera-1. Sequence ② controls Galvanometer-2, tasked with aiding the 3D reconstruction capabilities of Camera-2. Sequence ③ manages Galvanometer-3, which is responsible for active

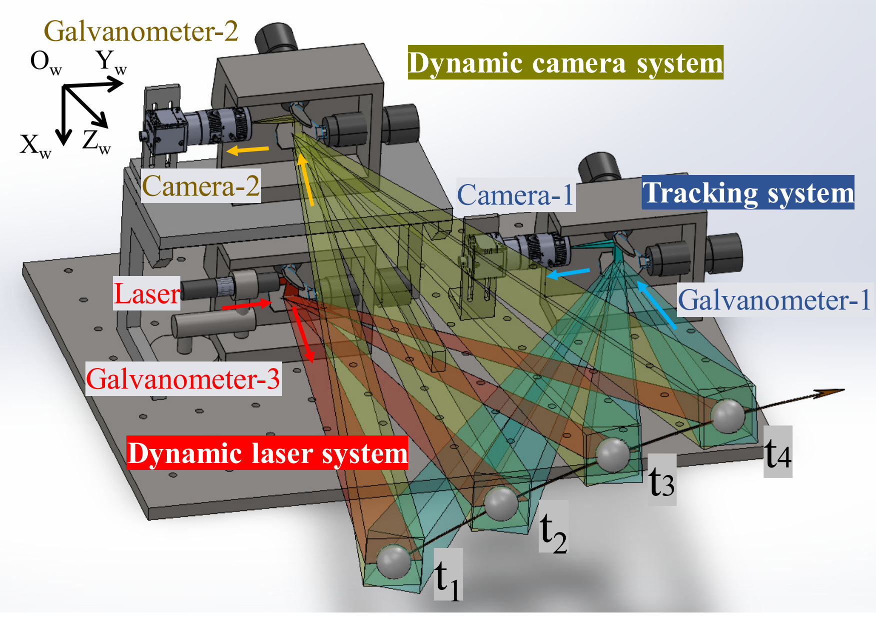

**Figure 5.2: System design of visual-feedback based active 3D reconstruction system.**

projection, and Sequence ④ is dedicated to the control of Camera-2. Notably, all three galvanometers operate in a coordinated manner within a synchronized control cycle of 10 ms. This cycle includes a 2 ms rotation time for accurate positioning, followed by a 5 ms delay to ensure stability before image capture. After this delay, Galvanometer-3 triggers a signal to Camera-2, initiating image capture. The 'stabilization time' for the galvanometers, following the camera trigger is set at 3 ms to ensure precise imaging conditions. Conversely, Camera-2's exposure time is finely tuned to 1 ms to capture sharp images with minimal motion blur. This meticulous synchronization of time intervals is critical for the system's ability to accurately capture and reconstruct images of moving objects.

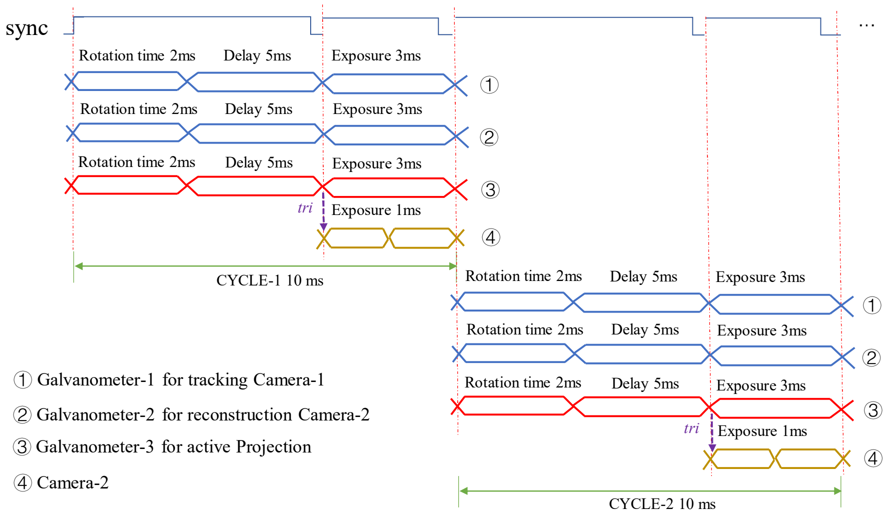

**Figure 5.3: Control sequence.**

## 5.4 Geometric Model

### 5.4.1 Tracking and Active 3D Reconstruction Model

The mathematical model is as shown in Figure. 5.4. In the model, $\{W\}$ is defined on the surface of the planar chessboard target, with the origin point O located at the upper-left corner of the planar. The X- and Y-axes are aligned with the direction of the chessboard array, while the Z-axis is perpendicular to the O-XY plane according to the right-hand coordinate system. $\{C_1\}$ and $\{C_2\}$ represent the coordinate systems of the cameras. The Z-axis of each camera corresponds to the corresponding optical axis, while the X- and Y-axes are aligned with the direction of the image plane following the right-hand coordinate frame. Similarly, $\{G_1\}$ and $\{G_2\}$ denote the coordinate systems of the galvanometers. The Z-axis of each galvanometer corresponds to the rotation axis of the pan mirror. The X-axis of $\{G_1\}$ corresponds to the optical axis of the camera, while the Y-axis is aligned with the line connecting the center points of the pan mirror and tilt mirror. For $\{G_3\}$, the Z-axis is oriented upward along the rotating shaft of the galvanometer. The X-axis is set according to the direction of the normal vector of the laser plane when the control voltage is at its initial value, and the Y-axis is determined based on the right-hand coordinate frame. According to the operating principle of the galvanometer, the rotation angle of the pan-tilt mirror is proportional to the applied voltage. Hence, for Galvanometer-1, the rotation angle of the pan-tilt mirror can be calculated using Eq. (5.1):

$$\begin{cases} \theta_1 = k_{1-pan} U_{1-pan}, \\ \theta_2 = k_{1-tilt} U_{1-tilt}, \end{cases} \tag{5.1}$$

Here, $k_{1-pan}$ and $k_{1-tilt}$ represent the scale factors of Galvanometer-1, which can be calculated based on the voltage range and angle range. A point in $\{W\}$ is represented as $P_i = \left(X_{p_i}, Y_{p_i}, Z_{p_i}\right)$, and its corresponding point in $\{V_1\}$ is denoted as $p_i = \left(x_{p_i}, y_{p_i}\right)$. The relationship between $p_i$ and the voltage of the galvanometer can be expressed as Eq. (5.2):

$$\begin{cases} \Delta U_{1-pan} = \alpha \Delta x_{p_i}, \\ \Delta U_{1-tilt} = \beta \Delta y_{p_i}, \end{cases} \tag{5.2}$$

$\Delta U_{1-pan}$ and $\Delta U_{1-tilt}$ represent the voltage offsets. $\Delta x_{p_i}$ and $\Delta y_{p_i}$ denote the offsets of the pixel coordinates of $p_i$. $\alpha$ and $\beta$ are offset factors that can be determined through calibration. The pixel offset of the object center between consecutive frames captured by Camera-1 can be calculated using an object detection algorithm. By applying Eq. (5.2), the control voltage for Galvanometer-1 can be calculated to ensure the tracking of the object by Subsystem-1. Based on the principle of light path reflection, the deflection angle of the light path is twice the deflection angle of the galvanometer mirror. Combining this with Eq. (5.1), in order to maintain point $P_i$ at the center of the virtual camera image, the relationship between the control voltage of the galvanometer mirror and observation point $P_i$ can be described by Eq. (5.3):

$$\begin{cases} U_{1-pan} = \frac{1}{2k_{1-pan}} \tan^{-1} \frac{X_{p_i}}{Z_{p_i}}, \\ U_{1-tilt} = \frac{1}{2k_{1-tilt}} \tan^{-1} \frac{Y_{p_i}}{Z_{p_i}}. \end{cases} \tag{5.3}$$

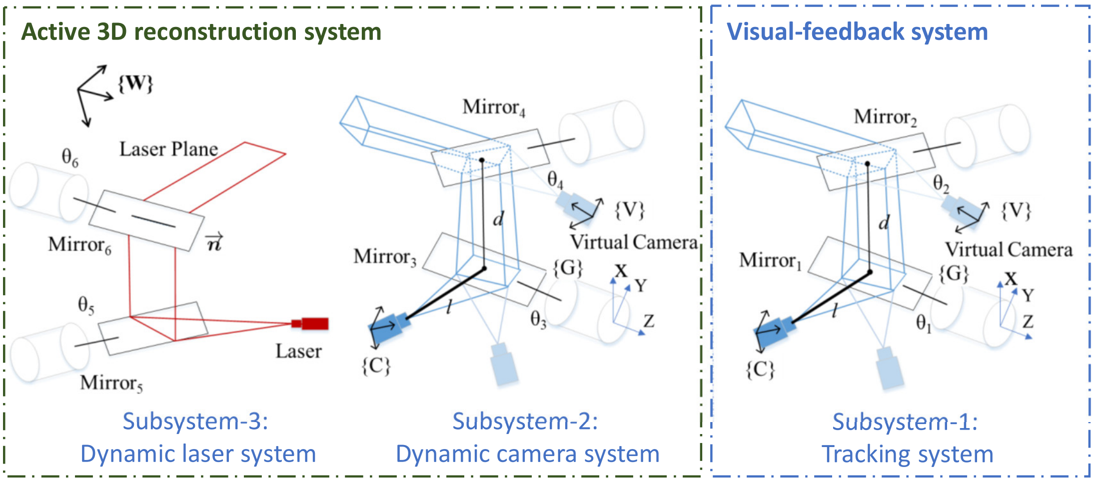

**Figure 5.4: Geometric model visual-feedback based active 3D reconstruction system.**

The same model as that in Eqs. (5.1), (5.2), and (5.3) is also applied to Galvanometer-2 and Galvanometer-3. Therefore, for the same observation point in $\{W\}$, the relationship between the voltages of Galvanometer-1, Galvanometer-2, and Galvanometer-3 can be described by Eq. (5.4) to maintain the observation point at the image center of the virtual camera:

$$\begin{aligned} \begin{bmatrix} U_{1-\mathrm{pan}} \\ U_{1-tilt} \\ 1 \end{bmatrix} &= \begin{bmatrix} a_1 & b_1 & c_1 \\ a_2 & b_2 & c_2 \\ 0 & 0 & 1 \end{bmatrix} \begin{bmatrix} U_{2-pan} \\ U_{2-tilt} \\ 1 \end{bmatrix} \\ &= \boldsymbol{T}_1 \begin{bmatrix} U_{2-pan} \\ U_{2-tilt} \\ 1 \end{bmatrix} = \boldsymbol{T}_2 \begin{bmatrix} U_{3-pan} \\ U_{3-\mathrm{tilt}} \\ 1 \end{bmatrix}. \end{aligned} \tag{5.4}$$

$$
{}^{\mathrm{V}_2}\mathbf{T}_{\mathrm{G}_2} = \begin{bmatrix} \sin 2\theta_3 & 0 & -\cos 2\theta_3 & l\cos 2\theta_3 \\ \cos 2\theta_3 \cos 2\theta_4 & \sin 2\theta_4 & \sin 2\theta_3 \sin 2\theta_4 & -l \sin 2\theta_3 \cos 2\theta_4 + d\,(1 - \cos 2\theta_4) \\ \cos 2\theta_3 \sin 2\theta_4 & -\cos 2\theta_4 & \sin 2\theta_3 \sin 2\theta_4 & -l \sin 2\theta_3 \sin 2\theta_4 - d \sin 2\theta_4 \\ 0 & 0 & 0 & 1 \end{bmatrix}. \tag{5.6}
$$

$\boldsymbol{T}_1$ and $\boldsymbol{T}_2$ are $3 \times 3$ matrices with six unknown parameters. According to Eq. (5.4), the tracking results of Subsystem-1 can be utilized to enable Subsystem-2 to capture the object image, and Subsystem-3 to project the laser stripe onto the object. As the pan-tilt mirror rotates, $\{V_2\}$ undergoes changes corresponding to variations in the voltages $U_{2-pan}$ and $U_{2-tilt}$. The relationship between $\{V_2\}$ and $\{V_{2-0}\}$ can be expressed as Eq. (5.5):

$$
\{\mathbf{V}_2\} = {}^{\mathrm{V}_2}\,\mathrm{T}_{\mathrm{V}_{2-0}}\,\{\mathbf{V}_{2-0}\} = {}^{\mathrm{V}_2}\mathrm{T}_{\mathrm{G}_2}{}^{G_2}\,\mathrm{T}_{\mathrm{V}_{2-0}}\,\{\mathbf{V}_{2-0}\}\,. \tag{5.5}
$$

As depicted in the geometric model diagram, $\{C_2\}$ undergoes reflection first by a pan-mirror and then by a tilt-mirror. The geometry of the two reflections is modeled by Eq. (5.6). When $U_{1-pan} = U_{1-tilt} = 0$, the rotation angles of the pan-tilt mirror for Galvanometer-2 are $\theta_3 = \theta_4 = 45°$. The transformation matrix ${}^{V_2}\mathrm{T}_{V_{2-0}}$ can be calculated using Eq. (5.7), representing the geometric model of the dynamic camera.

$$
{}^{\mathrm{V}_2}\,\mathrm{T}_{\mathrm{V}_{2-0}} = {}^{\mathrm{V}_2}\,\mathrm{T}_{G_2}{}^{\mathrm{V}_2}\,\mathrm{T}_{G_2}^{-1} \mid (\theta_3 = \theta_4 = 0)\,. \tag{5.7}
$$

The coordinates of the pixel point on the laser stripe are denoted as $(u, v)$. The coordinates of the corresponding 3D point in $\{V_2\}$ are denoted as $(X_V, Y_V, Z_V)$. The mapping relationship between them, based on the pinhole model of the camera, can be expressed as Eq. (5.8):

$$\begin{bmatrix} u \\ v \\ 1 \end{bmatrix} = \begin{bmatrix} f_x & 0 & u_0 & 0 \\ 0 & f_y & v_0 & 0 \\ 0 & 0 & 1 & 0 \end{bmatrix} \begin{bmatrix} R & T \\ 0^T & 1 \end{bmatrix} \begin{bmatrix} X_V \\ Y_V \\ Z_V \\ 1 \end{bmatrix}. \tag{5.8}$$

The initial laser plane in $\{V_{2-0}\}$ is denoted as ${}^{V_0}plane_0$, with the equation $A_0x+B_0y+C_0z+D_0=0$. The equation governing the rotation axis of the dynamic laser $\overrightarrow{\boldsymbol{n}}$ in $\{V_{2-0}\}$ can be written as $n_xx+n_yy+n_zz+d=0$. The laser plane after rotating by an angle $\theta$ around the rotation axis is denoted as ${}^{V_{2\text{-}0}}plane_0$, with the equation $A_{V_0}x+B_{V_0}y+C_{V_0}z+D_{V_0}=0$. The light from the dynamic laser is reflected by the mirror and rotates along with the mirror's rotation. The rotation angle of the laser plane is twice the rotation angle of the mirror. Therefore, the equation of the dynamic laser plane after rotation in the $\{V_{2-0}\}$ can be expressed as Eq. (5.9):

$$\begin{bmatrix} A_{V_0} \\ B_{V_0} \\ C_{V_0} \end{bmatrix} = R\left(\overrightarrow{\mathbf{n}}, 2\theta_6\right) \begin{bmatrix} A_0 \\ B_0 \\ C_0 \end{bmatrix}. \tag{5.9}$$

Where $\boldsymbol{R}$ represents the Rodrigues transformation. By selecting a point $(x_n, y_n, z_n)$ on the rotation axis, $D_{V_0}$ can be calculated as $D_{V_0}=-A_{V_0}x_n-B_{V_0}y_n-C_{V_0}z_n$. By combining ${}^{V_{2\text{-}0}}plane_0$ and Eq. (5.7), the equation of the dynamic laser plane in $\{V_2\}$, denoted as ${}^{V_2}plane_0$, can be computed. The equation is represented as $A_Vx+B_Vy+C_Vz+D_V=0$. By extracting the pixel points $(u, v)$ on the laser stripe, the corresponding 3D point can be denoted as ${}^{V_2}\boldsymbol{P}=(X_V, Y_V, Z_V)$. Thus, the relationship between ${}^{V_2}\boldsymbol{P}$ and the change in the galvanometer mirror angle can be expressed as Eq. (5.10):

$$\begin{cases} Z_V = D_V / \left[ A_V \times (u - u_0) / f_x + B_V \times (v - v_0) / f_y + C_V \right] \\ X_V = (u - u_0) / f_x \times Z_V \\ Y_V = (v - v_0) / f_y \times Z_V \\ \{A_V, B_V, C_V, D_V\} = \boldsymbol{F}\left(\theta_3, \theta_4, \theta_5, \theta_6; A_0, B_0, C_0, D_0, l, d, \vec{\mathbf{n}}, \mathbf{P}\right) \\ \{\theta_3, \theta_4, \theta_5, \theta_6\} = \boldsymbol{G}\left(U_{1-pan}, U_{1-tilt}; \mathbf{T}_1, \mathbf{T}_2, \alpha, \beta\right) \end{cases} \tag{5.10}$$

Since $\{V_2\}$ changes constantly with the scanning angle, it is necessary to transform all ${}^{V_2}\boldsymbol{P}$ points into a coordinate system that remains fixed with the world coordinates system $\{W\}$. For convenience, we select $\{V_{2-0}\}$ as the reference coordinate system and obtain ${}^{V_{2-0}}\boldsymbol{P} = (X_{V_0}, Y_{V_0}, Z_{V_0}) = {}^{V_{2-0}}\boldsymbol{T}_{V_2}{}^{V_2}\boldsymbol{P}$. This establishes the relationship between $(u, v)$ and ${}^{V_0}\boldsymbol{P}$, enabling complete 3D reconstruction of the moving object.

### 5.4.2 3D Motion Compensation Model

In the process of object motion, Camera-1 tracks the target, with the acquired image denoted as $I_1$. The center of the image is represented as $(I_{1x}, I_{1y})$, while the center of the bounding box of the target within $I_1$ is denoted as $(O_{1x}, O_{1y})$. The height of the bounding box is represented as $h$. Concurrently, the laser conducts periodic scanning on the object following the algorithm presented in Algorithm 2. If the target remains stationary, the complete point cloud of the target can be reconstructed based on the above mathematical model. However, due to the target's displacement between each image frame, the reconstructed point cloud will contain 3D errors, as illustrated in Fig. 5.1(a). Hence, 3D motion compensation is necessary to rectify the reconstruction and obtain accurate results. The coordinates of the target center on the motion plane are denoted as $(x_n, y_n)$, and their relationship with the Galvanometer-1 voltage is described by Eq. (5.11):

$$\begin{cases} x_n = s_{pan} U_{pan-1} + t_{pan} \\ y_n = s_{tilt} U_{tilt-1} + t_{tilt}. \end{cases} \tag{5.11}$$

Here, $s_{pan}, t_{pan}, s_{tilt}, t_{tilt}$ are linear parameters. The coordinates of the target center in $\{V_{2-0}\}$ is denoted as $(X_n, Y_n, Z_n)$. The relationship between $(x_n, y_n)$ and $(X_n, Y_n, Z_n)$ can be expressed by Eq. (5.12):

$$\begin{bmatrix} X_n \\ Y_n \\ Z_n \\ 1 \end{bmatrix} = \begin{bmatrix} n_x & o_x & a_x & t_x \\ n_y & o_y & a_y & t_y \\ n_z & o_z & a_z & t_z \\ 0 & 0 & 0 & 1 \end{bmatrix} \begin{bmatrix} x_n \\ y_n \\ 0 \\ 1 \end{bmatrix} = \mathbf{T_3} \begin{bmatrix} x_n \\ y_n \\ 0 \\ 1 \end{bmatrix}. \tag{5.12}$$

**Algorithm 2** Tracking and Scanning algorithm

```
Initialize: $i \leftarrow 0, I_{1x}, I_{1y}$.
$(O_{1x}, O_{1y}, h) \leftarrow Detection(Image)$
if $Image\ contains\ objects$ then
    while $(\Delta pixel_y < O_{1x} - I_{1y} + 0.5h)$ do
        $\Delta pixel_x \leftarrow O_{1x} - I_{1x}$
        $\Delta pixel_y \leftarrow O_{1y} - I_{1y} - 0.5h + i$
        $i \leftarrow i + 1$
        $U_{1-pan} \leftarrow k_{1-pan} \Delta pixel_x + u_0$
        $U_{1-tilt} \leftarrow k_{1-tilt} \Delta pixel_y + v_0$
        $[U_{3-pan}, U_{3-tilt}, 1]^T \leftarrow \mathbf{T_3}[U_{1-pan}, U_{1-tilt}, 1]^T$
    end while
end if
```

Thus, the displacement generated by the motion can be calculated as $d = (X_n - X_{n_0}, Y_n - Y_{n_0}, Z_n - Z_{n_0})$. The point cloud after 3D motion compensation is denoted as ${}^{V_{2-0}}\boldsymbol{P'} = (X_{V_0} + dx, Y_{V_0} + dy, Z_{V_0} + dz)$. In the mathematical model of the tracking and dynamic 3D system described by Eqs. (5.10), (5.11), and (5.12), the parameters $f_x$, $f_y$, $u_0$, $v_0$ can be obtained from camera calibration, while $A_0$, $B_0$, $C_0$, $D_0$ can be obtained from the laser plane calibration method. The parameters $\alpha, \beta$, $l$, $d$, $\overrightarrow{\boldsymbol{n}} = (n_x, n_y, n_z)$, $\boldsymbol{P} = (X_0, Y_0, Z_0)$, $s_{pan}$, $t_{pan}$, $s_{tilt}$, $t_{tilt}$, $\mathbf{T_1}$, $\mathbf{T_2}$, $\mathbf{T_3}$ are unknown, and a calibration algorithm should be designed to obtain them.

## 5.5 Calibration Method

The system calibration method proposed in this study comprises four steps, as shown in Fig. 5.5: active 3D reconstruction system calibration, tracking system calibration, joint calibration of tracking and active 3D system, and 3D movement compensation calibration. The color-coded titles in Fig. 5.5 correspond to the hues presented in Fig. 5.1(b), with the parameters derived from each calibration step being employed in the respective color-matched workflow. The active 3D reconstruction involves dynamic camera calibration, dynamic laser calibration, and joint calibration of the dynamic camera and dynamic laser. These calibrations ensure that accurate and reliable 3D information can be calculated. The tracking system calibration establishes the relationship between Subsystem-1 and the $\{W\}$ coordinate system, enabling Subsystem-1 to track the object accurately. The joint calibration of the tracking and active 3D system establishes the relationship between Subsystem-1, Subsystem-2, and Subsystem-3, allowing Subsystem-3 to project the laser stripe onto the object and Subsystem-2 to capture the object image based on the tracking results. The 3D movement compensation calibration corrects the 3D motion errors caused by the object's movement. After completing all the calibration steps, the system is ready to be used for tracking and active 3D reconstruction of moving objects, providing enhanced accuracy and performance.

### 5.5.1 Active 3D Reconstruction Calibration

For the calibration of the active 3D reconstruction system, the first step is to calibrate the camera's intrinsic parameters, including $f_x$, $f_y$, $u_0$, and $v_0$. We adopt the method

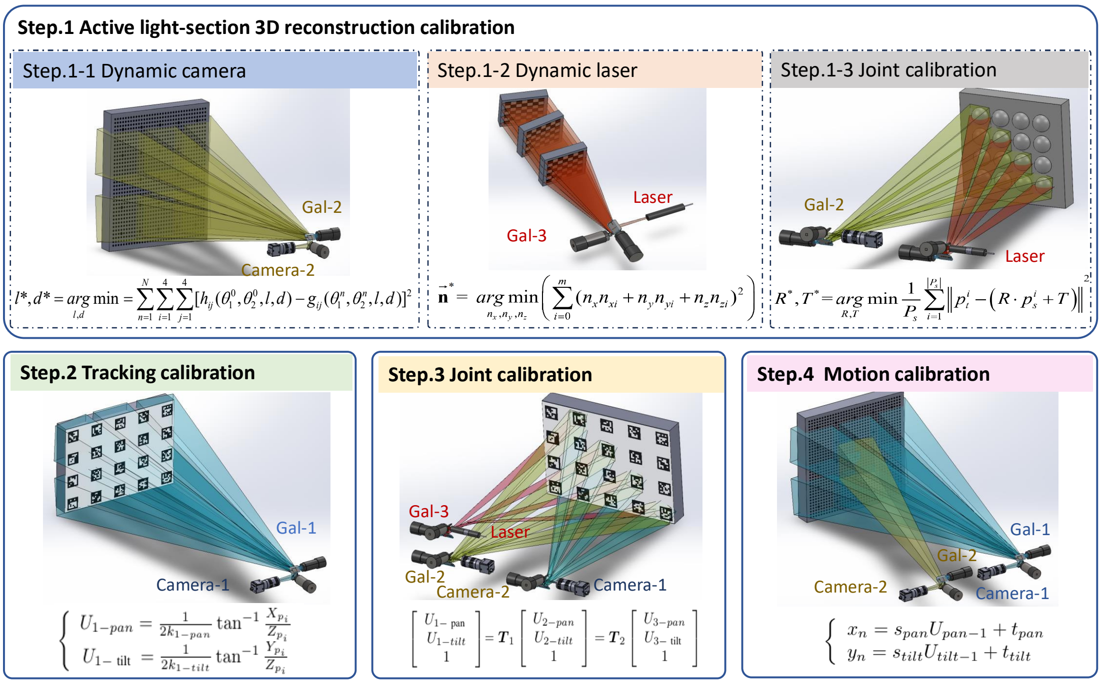

**Figure 5.5: Calibration method of visual-feedback-based active light-section 3D reconstruction system. Step 1. Active light-section 3D reconstruction system calibration includes Steps 1-1. dynamic camera calibration, Steps 1-2. dynamic laser calibration, and Steps 1-3, joint calibration of dynamic camera and laser. Step 2. Tracking system calibration. Step 3. Joint calibration of active light-section 3D reconstruction and tracking. Step 4. 3D motion compensation calibration.**

proposed by Zhang [**?**] for this purpose. Next, we perform dynamic camera calibration to determine the relationship between the coordinate frames $\{V_2\}$ and $\{G_2\}$. Specifically, we aim to obtain the parameters $l$ and $d$ in Eq. (5.10). Our proposed calibration method utilizes a large calibration board. By scanning the calibration board while varying the voltage of Galvanometer-2, we acquire a significant number of images of the board at different galvanometer rotation angles, with each image corresponding to a virtual coordinate system. We denote the number of these images as $n$. The conversion matrices between $\{V_2\}$ and $\{W\}$ can be obtained through extrinsic parameter calibration, denoted as ${}^{V_{2-0}}\boldsymbol{T}_W$, ${}^{V_{2-1}}\boldsymbol{T}_W$, ${}^{V_{2-2}}\boldsymbol{T}_W,\ldots,{}^{V_{2-n}}\boldsymbol{T}_W$. Given the known relative positions between the calibration points in the images, we can calculate the transformation matrices between the virtual coordinate systems as ${}^{V_{2-1}}\boldsymbol{T}_{V_{2-0}}$, ${}^{V_{2-2}}\boldsymbol{T}_{V_{2-0}},\ldots,$ ${}^{V_{2-n}}\boldsymbol{T}_{V_{2-0}}$. These values serve as observations for the calibration process. By utilizing multiple sets of observations, we can solve for the parameters to be calibrated. The initial pan-tilt angles of Galvanometer-2 are denoted as $\theta_3(0)$ and $\theta_4(0)$, which are the corresponding angles of $\{V_0\}$ and the first calibration image. The pan-tilt angles of Galvanometer-2 corresponding to $\{V_{2-n}\}$ and $n$ calibration images are denoted as $\theta_3(n)$ and $\theta_4(n)$. Therefore, $\{V_{2-0}\}$ and $\{V_{2-n}\}$ can be represented as follows:

$$\begin{aligned} \{V_{2-0}\} &= k_{ij}(\theta_3^{(0)}, \theta_4^{(0)}, l, d), \\ \{V_{2-n}\} &= g_{ij}(\theta_3^{(n)}, \theta_4^{(n)}, l, d), \end{aligned} \tag{5.13}$$

where $k_{ij}$ and $g_{ij}$ represent the function of $\{V_{2-0}\}$ and $\{V_{2-n}\}$, respectively, and $l$ and $d$ are the parameters to be calibrated. The transformation matrix between $\{V_{2-0}\}$ and $\{V_{2-n}\}$ is a 4×4 matrix denoted as ${}^{V_{2-n}}\mathbf{T}_{V_{2-0}}(n)a_{ij}^{n}$. Additionally, $\{V_{2-n}\}$ can be calculated based on $\{V_{2-0}\}$ in Eq. (5.13) and ${}^{V_{2-n}}\boldsymbol{T}_{V_{2-0}}$. For simplicity of notation, we denote this relationship as a function $h_{ij}$:

$$\begin{aligned} &\{V_{2-n}\} = {}^{V_{2-n}}\boldsymbol{T}_{V_{2-0}}(n) \cdot \{V_{2-n}\} = \\ &\sum_{i=1}^{4}\sum_{j=1}^{4} a_{ij}^{n} k_{ij}\left(\theta_3^{(0)}, \theta_4^{(0)}, l, d\right) = h_{ij}\left(\theta_3^{(0)}, \theta_4^{(0)}, l, d\right). \end{aligned} \tag{5.14}$$

In the proposed calibration framework, $\{G_2\}$ serves as the base coordinate frame, and $\{V_2\}$ is defined as $\{V_2\} = {}^{V_2}\boldsymbol{T}_{G_2} \cdot \{G_2\}$. Therefore, Eq. (5.6) also represents the mathematical model of $\{V_2\}$. Eq. (5.13) represents the obtained result of $\{V_2\}$ from multiple observations. Eq. (5.14) represents the result calculated based on the mathematical model of the dynamic camera. To ensure the accuracy of calibration, the objective is to minimize the sum of errors between the theoretical and measured values for all observed coordinate frames, including $\{V_{2-0}\}$, $\{V_{2-1}\}$, $\{V_{2-2}\}$,..., $\{V_{2-n}\}$. Thus, an objective function can be formulated as shown in Eq. (5.15). By solving this objective function, we can complete the dynamic camera calibration.

$$\begin{aligned} l^*, d^* = \arg\min_{l,d} & \sum_{n=1}^{N} \sum_{i=1}^{4} \sum_{j=1}^{4} \\ & \left[h_{ij}\left(\theta_3^0, \theta_4^0, l, d\right) - g_{ij}\left(\theta_3^n, \theta_4^n, l, d\right)\right]^2 . \end{aligned} \tag{5.15}$$

Furthermore, we conduct dynamic laser calibration to calibrate the equation governing ${}^{V_{2-0}}plane_0$ and determine the rotation axis of the dynamic laser $\overrightarrow{\boldsymbol{n}}$. For ${}^{V_0}plane_0$, we employ the calibration method described in [**?**], which involves using a checkerboard calibration plate and capturing laser images at multiple positions. By fitting the laser plane using multiple laser lines, we can obtain the equation $A_0x + B_0y + C_0z + D_0 = 0$ for ${}^{V_0}plane_0$.

By changing the voltage of Galvanometer-3 $U_{3-tilt} = U_1, U_2, ..., U_m$, we can induce the movement of the laser and obtain multiple laser planes. Similar to the calibration process for ${}^{V_{2-0}}plane_0$, we calibrate the equations of these laser planes and denote them as ${}^{V_{2-0}}plane_1, {}^{V_{2-0}}plane_2, ..., {}^{V_{2-0}}plane_m$. From each plane, we calculate the unit normal vectors denoted as $\overrightarrow{\boldsymbol{n}}_0(n_{x_0}, n_{y_0}, n_{z_0})$, $\overrightarrow{\boldsymbol{n}}_1(n_{x_1}, n_{y_1}, n_{z_1})$, $\overrightarrow{\boldsymbol{n}}_2(n_{x_2}, n_{y_2}, n_{z_2})$,..., $\overrightarrow{\boldsymbol{n}}_m(n_{x_m}, n_{y_m}, n_{z_m})$. In the absence of errors, these laser planes should intersect at the same straight line representing the laser rotation axis $\overrightarrow{\boldsymbol{n}} = (n_x, n_y, n_z)$. This axis also corresponds to the rotation axis of the tilt-mirror in Galvanometer-3. Ideally, the dot product between the laser rotation axis and any normal vector from the laser planes should be zero, that is, $\overrightarrow{\boldsymbol{n}} \cdot \overrightarrow{\boldsymbol{n}}_i = 0$ (for $i = 0, 1, 2, ..., m$). However, due to errors, the dot product $\overrightarrow{\boldsymbol{n}} \cdot \overrightarrow{\boldsymbol{n}}_i$ is not exactly zero. To account for these errors, we have designed an objective function as shown in Eq. (5.16), which aims to minimize the sum of squares of the dot products between the laser rotation axis and normal vectors of all laser planes.

$$\overrightarrow{\mathbf{n}}^{*} = \underset{n_x,n_y,n_z}{\arg\min}\left(\sum_{i=0}^{m}\left(n_x n_{x_i} + n_y n_{y_i} + n_z n_{z_i}\right)^2\right). \tag{5.16}$$

The direction vector $\overrightarrow{\boldsymbol{n}}$ of the rotation axis can be obtained by minimizing the objective function. $\boldsymbol{P} = (X_0, Y_0, Z_0)$ represents a point on the rotation axis that lies in all laser planes, and can be obtained using the least squares method.

Following the calibration of the dynamic camera and laser system, all the parameters in Eq. (5.10) are determined, enabling the extraction of accurate 3D information. In principle, during the scanning process of Galvanometer-1 while Galvanometer-2 remains stationary, the reconstructed laser point clouds should align perfectly. However, due to inherent system errors, slight deviations exist among the multiple laser point clouds. To rectify these deviations, point-cloud registration techniques were employed, leading to the derivation of a precise transformation matrix utilizing a calibration sphere. By performing a joint calibration of the dynamic camera and laser system to address the identified errors, we successfully achieved the comprehensive calibration of the active 3D reconstruction system.

### 5.5.2 Tracking System Calibration

Tracking system calibration aims to determine the offset factors $\alpha$ and $\beta$. To achieve this, we select an arbitrary point $\boldsymbol{P}$ in space, and denote its corresponding pixel coordinates in Camera-1 as $\boldsymbol{P}_0(x_0, y_0)$, with Galvanometer-1's voltage being $U_{10}(U_{pan-10}, U_{tilt-10})$. By varying the voltage of Galvanometer-1 to $U_{11}(U_{pan-11}, U_{tilt-11})$, $U_{12}(U_{pan-12}, U_{tilt-12})$,..., $U_{1n}(U_{pan-1n}, U_{tilt-1n})$, we can obtain the corresponding coordinates of point $\boldsymbol{P}$ in $\{V_1\}$ as $\boldsymbol{P}_1(x_1, y_1)$, $\boldsymbol{P}_2(x_2, y_2)$,..., $\boldsymbol{P}_n(x_n, y_n)$. By utilizing Eq. (5.17), we can calculate the parameters $\alpha$ and $\beta$ for the tracking system calibration process.

$$\begin{cases} \alpha = \dfrac{1}{n} \displaystyle\sum_{i=1}^{n} \dfrac{x_i - x_0}{U_{pan-1i} - U_{pan-1i}}, \\ \beta = \dfrac{1}{n} \displaystyle\sum_{i=1}^{n} \dfrac{y_i - y_0}{U_{tilt-1i} - U_{tilt-1i}}. \end{cases} \tag{5.17}$$

### 5.5.3 Joint Calibration of Tracking and Active 3D Reconstruction

A set of $n$ points in $\{W\}$ is selected (where $n > 6$). With the calibrated values of $\alpha$ and $\beta$, the galvanometer voltage can be calculated to ensure that these points are centered in the imaging of $\{V_1\}$, $\{V_2\}$, and $\{V_3\}$ simultaneously. The voltage values for Galvanometer-1 are denoted as $U_{11}(U_{pan-11}, U_{tilt-11})$, $U_{12}(U_{pan-12}, U_{tilt-12})$,..., $U_{1n}(U_{pan-1n}, U_{tilt-1n})$. The voltage values for Galvanometer-2 are denoted as $U_{21}(U_{pan-21}, U_{tilt-21})$, $U_{22}(U_{pan-22}, U_{tilt-22})$,..., $U_{2n}(U_{pan-2n}, U_{tilt-2n})$. The voltage values for Galvanometer-3 are denoted as $U_{31}(U_{pan-31}, U_{tilt-31})$, $U_{32}(U_{pan-32}, U_{tilt-32})$,..., $U_{3n}(U_{pan-3n}, U_{tilt-3n})$. By inputting these data into Eq. (5.4) and using the least-square method, the matrices $\mathbf{T_1}$ and $\mathbf{T_2}$ can be calculated.

### 5.5.4 3D Motion Compensation Calibration

For the calibration of 3D motion compensation parameters, namely $s_{pan}$, $t_{pan}$, $s_{tilt}$, and $t_{tilt}$, we utilize a calibration board equipped with circular calibration points. Virtual Camera-1 captures the pixel coordinates of each circle's center on the calibration board: $O_1(x_1, y_1), O_2(x_2, y_2), ..., O_n(x_n, y_n)$. By utilizing Eq. (5.2), the voltages needed to align each circle's center with the imaging center can be computed: $U_{11}(U_{pan-11}, U_{tilt-11})$,$U_{12}(U_{pan-12}, U_{tilt-12})$,..., $U_{1n}(U_{pan-1n}, U_{tilt-1n})$. By inputting the circle center coordinate values and the corresponding pan-tilt mirror voltage values into Eq. (5.11) and applying the least squares method, $s_{pan}$, $t_{pan}$, $s_{tilt}$, and $t_{tilt}$ can be calculated. Zhang's [?] calibration method is utilized to calibrate the external parameters of $V_{2-0}$ with respect to the calibration board coordinate system, thereby yielding $\mathbf{T}_3$. Calibrating the tracking system, projecting system, active 3D system, and 3D motion compensation completes the necessary processes of the proposed visual-feedback based active 3D reconstruction system.

## 5.6 Experiment

The proposed visual-feedback active light-section 3D reconstruction system was constructed as shown in Fig. 5.6. The camera model was MV-CA004-10UC, with a pixel size of 6.9 $\mu$m × 6.9 $\mu$m, resolution of 720 pixels × 540 pixels, and frame rate of 500 fps. The exposure time of the Camera-1 was 5000 $\mu$s in capturing the light information of the tracked object. The exposure time of Camera-2 was 500 $\mu$s in capturing the dark image of the laser with a wavelength of 650 nm. Galvanometer-1, Galvanometer-2, and Galvanometer-3 used were of model TSH8310. The galvanometer was used to scan a ±20° range using a control voltage range of $-10V - +10V$. The maximum scan frequency was 1 kHz, with an angular resolution of 0.0008; thus, the system has the potential for high accuracy and resolution.

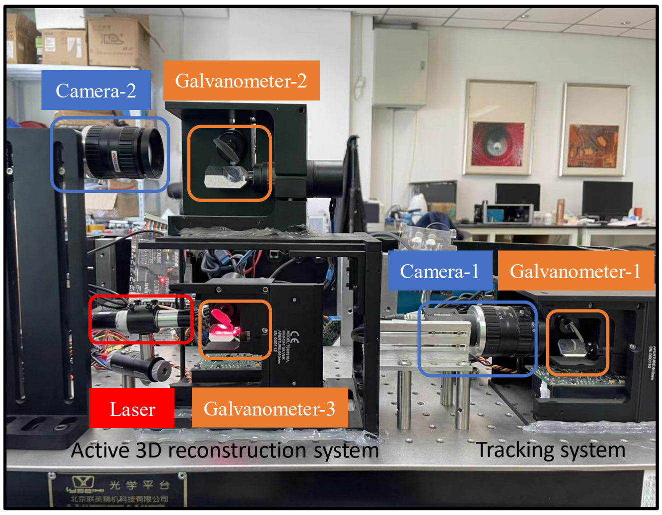

**Figure 5.6: Visual-feedback active light-section 3D reconstruction system.**

## 5.6.1 Moving Laser Imaging Accuracy Verification

In the experiments, we first validate the design of the control sequence under the proposed method, particularly focusing on its ability to capture clear images of a moving line laser without motion blur. Specifically, we test the system by driving the line laser to move at a speed of 90 lines per second while simultaneously moving the camera to capture the laser images. The scanning step of the galvanometer is set at 0.03V. A total of 45 laser lines are collected for analysis. We examine the grayscale distribution of these moving laser lines to understand the uniformity and clarity of the laser lines across different positions. The results reveal that each laser line is approximately 10 pixels wide and exhibits a distinct peak in grayscale values. This indicates that the proposed system successfully captures clear images of the moving line laser, thereby facilitating the precise extraction of the laser center using a laser center extraction algorithm. These results demonstrate the control sequence's capability to effectively reduce motion blur, thereby enhancing the clarity of images for moving objects.

## 5.6.2 System Calibration

### 5.6.2.1 Active 3D reconstruction calibration

A total of 25 images of the calibration board were captured by Camera-2 at a Galvanometer-2 voltage of (0, 0). The camera intrinsic parameter calibration process was performed using the Zhang calibration method available in OpenCV. Following calibration, the intrinsic parameters were determined as $f_x = 7801.375$, $f_y = 7798.242$, $u_0 = 359.5$, $v_0 = 269.5$. By applying the calibration method for dynamic cameras described in Part III, the system parameters were derived as $l = 83.45$ mm and $d = 22.14$ mm.

To proceed with the calibration, the Galvanometer-2 tilt mirror was fixed, and the calibration board was positioned within the FOV of the virtual camera. The tilt mirror of Galvanometer-2 was then controlled to rotate 30 times with a step size of 0.1 V while scanning the calibration board. Additionally, the position of the calibration board was randomly changed five times to ensure clear imaging in the virtual camera. This process was repeated for 30 scans. The laser rotation axis were determined as $(\vec{\mathbf{n}}, \mathbf{P}) = ([0.99, 0.02, -0.0004], [-18310.30, -195.93, 257.97])$.

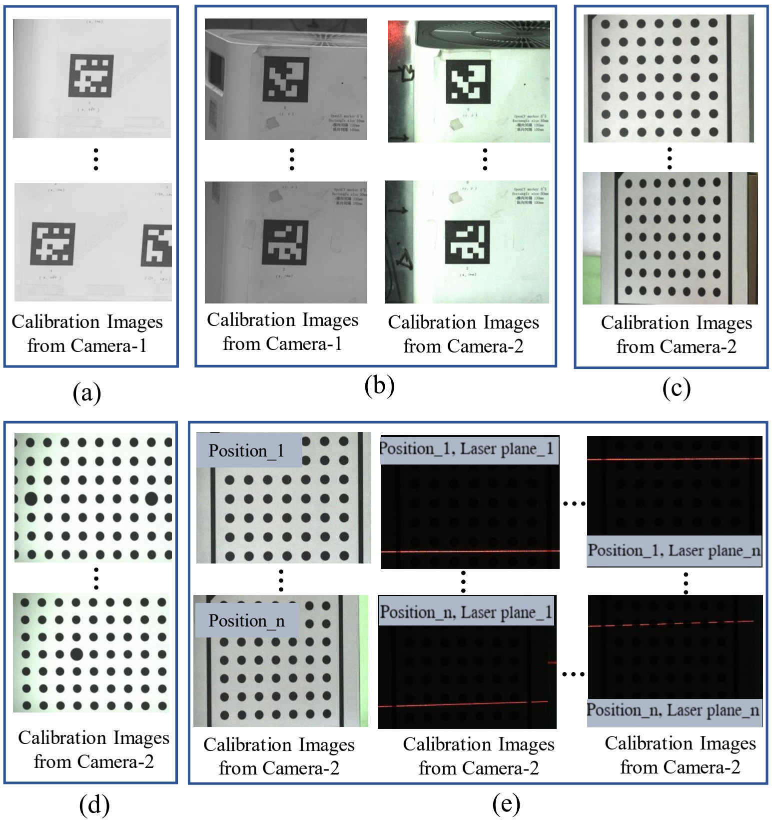

**Figure 5.7: Calibration images. (a) Calibration of Camera-1 and Galvanometer-1 for active tracking. (b) Calibration of Galvanometer-1 and Galvanometer-2,3 for active projecting. (c) Calibration intrinsic matrix of Camera-2. (d) Calibration geometric relationship of Camera-2 and Galvanometer-2 for active 3D reconstruction. (d) Calibration geometric relationship of laser and Galvanometer-3 for active 3D construction.**

#### 5.6.2.2 Tracking system calibration

Ten images of a QR code marker are captured by Camera-1 at ten different voltage levels of Galvanometer-1 denoted as $U_{1-i}$. A marker detection algorithm is used to obtain the pixel coordinates of the marker center $(x_i, y_i)$. These data are then used to calibrate the parameters in Eq. (5.17), resulting in the values $\alpha$ = -0.0182482 and $\beta$ = -0.0188679.

#### 5.6.2.3 Joint calibration of tracking and active 3D system

The same QR code marker calibration board used previously is employed. Galvanometer-1 and Galvanometer-2 are controlled to scan this calibration board, and the markers are detected. According to Eq. (5.3), the voltage values $U_{1-0}, U_{1-2}, ..., U_{1-9}$ and $U_{2-0}, U_{2-2}, ..., U_{2-9}$ at which the centers of these ten markers are aligned with the centers of Camera-1 and Camera-2 images, respectively, are computed. By substituting these values into Eq. (5.4), the transformation matrix $\mathbf{T}_1$ can be solved.

$$\mathbf{T}_1 = \begin{bmatrix} 0.99599012 & 0.03435418 & -2.54364167 \\ -0.01393105 & 0.96893803 & 1.12522601 \\ 0 & 0 & 1 \end{bmatrix}. \tag{5.18}$$

#### 5.6.2.4 3D motion compensation calibration

Galvanometer-1 was controlled to scan the large calibration board shown in Fig. 5.5. The size of the calibration board was 740 mm × 740 mm, and it contained 25 large circular markers. The distance between the large circular markers was 140 mm. By utilizing the pixel coordinates of the large circular markers and their corresponding scanning voltages, the voltages required to align the centers of the large circular markers with the image centers were calculated. The relationship parameters between $\{G_2\}$ and $\{W\}$ were determined as follows: $s_{pan} = 77.77$, $s_{tilt} = 70.00$, $t_{pan} = -314.00$, $t_{tilt} = 142.55$. While keeping Galvanometer-2 at its initial position, we applied the Zhang calibration method in OpenCV to compute the extrinsic matrix $\mathbf{T}_3$ between the calibration board coordinate system and $\{V_2\}$.

$$\mathbf{T}_3 = \begin{bmatrix} 1.29e-03 & 0.999 & -0.04527 & -25.9 \\ 1 & -9.64e-04 & 7.23e-03 & -22.4 \\ 7.18e-03 & -0.04527 & -0.9989 & 996.4 \\ 0 & 0 & 0 & 1 \end{bmatrix}. \quad (5.19)$$

All parameters in Eq. (5.10), (5.11), and (5.12) are computed, completing the system calibration process. In the next section, we will describe experiments using the proposed visual-feedback-based active 3D system to perform 3D measurements on moving objects and evaluate the accuracy of the calibration.

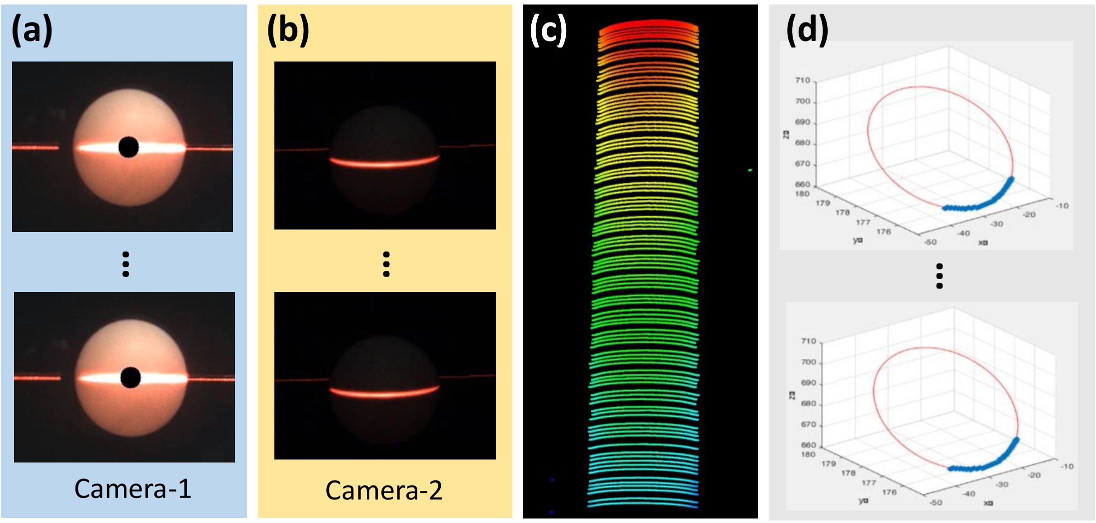

**Figure 5.8: 3D recontruction of moving ceramic sphere with single laser stripe. (a) Image sequence of Camera-1. (b) Image sequence of Camera-2. (c) The 3D point cloud of moving ceramic sphere. (d) Circle fitting of each point cloud.**

### 5.6.3 Accuracy Evaluation

To assess the feasibility and accuracy of the proposed system, we conducted two experiments. The first experiment aimed to evaluate the precision of tracking, projection, and 3D reconstruction for moving objects. Therefore, we tested the 3D reconstruction accuracy of a moving object using a single laser stripe at different speeds. In the second experiment, we further validated the 3D reconstruction accuracy after scanning and applying 3D motion compensation to the moving object. We completed the 3D reconstruction of the object by simultaneously tracking and scanning the object with laser stripes at different speeds. Then, we used the 3D motion compensation method to correct motion errors, and tested the overall reconstruction accuracy of the object.

#### 5.6.3.1 Accuracy test for 3D reconstruction with single laser stripe at different speeds

A standard ceramic sphere with a diameter of 20 mm was used for measurements at four different speeds. To control the sphere's motion speed for quantitative analysis, a linear slider was employed, allowing the sphere to move at speeds of 100 mm/s, 200 mm/s, 500 mm/s, and 1000 mm/s. Camera-1 detected the target, and the laser stripe was projected onto the center of the sphere, as shown in Fig. 5.8(a), which represents the image sequence captured by Camera-1. Camera-2 captured the dark laser stripe image, as shown in Fig. 5.8(b), and the resulting reconstructed point cloud is presented in Fig. 5.8(c). Each laser stripe's point cloud was fitted to calculate the diameter of the circle, as shown in Fig. 5.8(d).

To verify the effectiveness and accuracy of the proposed calibration method, we compared the actual diameter of the ceramic sphere with the fitted diameter obtained from the 3D point clouds. The error between the actual value and fitted value were calculated at each design speed. The mean, max, and root mean square error (RMSE) are presented in Table 5.1. The results indicate that the RMSE values at different speeds are within 0.2 mm, demonstrating the high precision and stability of the measurement for the proposed system. Furthermore, the consistent RMSE values at different speeds indicate the high robustness of the proposed system.

**Table 5.1: Mean, Max and RMSE Error of Fitting Circle Diameter**

| Speed/mm·s$^{-1}$ | 0 | 100 | 200 | 500 | 1000 |
|---|---|---|---|---|---|
| Mean Error /mm | 0.0821 | 0.1147 | 0.1654 | 0.1379 | 0.1032 |
| Max Error /mm | 0.1043 | 0.1184 | 0.1725 | 0.1441 | 0.1127 |
| RMSE /mm | 0.0962 | 0.1265 | 0.1175 | 0.1858 | 0.1547 |

#### 5.6.3.2 Accuracy test for scanning and 3D motion compensation at different speeds

The standard ceramic stair, standard ceramic sphere, and linear slider were used in this experiment. As in the previous experiment, the object was also moved at speeds of 100 mm/s, 200 mm/s, 500 mm/s, and 1000 mm/s. Subsystem-1 was used for tracking the object, while Subsystem-3 controlled the laser stripe to scan the object circle by circle. Subsystem-2 captured the images for 3D reconstruction. Fig. 5.10 presents the results of 3D reconstruction and 3D motion compensation for the moving object at different speeds. It can be observed that, theoretically, the intervals between adjacent scan slices in the 3D point cloud's layer slicing should be consistent due to the uniform scanning speed. However, some intervals appear larger, which is attributed to frame drops during the tracking of the moving object. Increasing the camera's frame rate can ameliorate this issue.

To verify the accuracy, the object was reconstructed repeatedly from ten positions at each designed speed. The 3D point cloud of the stair and sphere was fitted after 3D motion compensation. The distance of the stair and the diameter of the sphere were calculated. The error between the actual distance/diameter and fitted distance/diameter of the ceramic stair/sphere is illustrated in Fig. 5.9. The mean error, max error, and RMSE of the moving object at different speeds are calculated and presented in Table 5.2. When the object was stationary, the repeated measurement error ranged between 0.0124 mm and 0.1086 mm, with an RMSE of 0.0845 mm. In contrast, when the object was in motion at different speeds, the repeated measurement error varied from 0.2232 mm to 0.5993 mm, with the RMSE remaining below 0.5 mm. These results demonstrate the high precision and stability of our system in measuring moving objects. Analysis of the errors from corresponding points at each position indicates that the error slightly increases with speed. This can be attributed to the fact that at higher speeds, the object covers a larger distance during one scanning cycle, resulting in accumulated errors in 3D motion compensation. Enhancing the image capture speed of the system could further improve its accuracy, particularly at higher object speeds. Moreover, a limitation of this system is that the 3D motion errors caused by the object's movement in the depth direction of the camera cannot be effectively compensated by the methods described in the paper, thus affecting the reconstruction accuracy. To address this issue, increasing the scanning speed of the system could be beneficial, as shortening the scanning cycle time could reduce the generation of errors.

## 5.7 Concluding Remarks

In this study, a novel 3D reconstruction method for moving objects based on the light-section technique is proposed. This method integrates visual feedback from tracking results to ensure the object remains stationary relative to the 3D reconstruction system during movement. A comprehensive mathematical model of the system is established, and a flexible and accurate calibration method is developed.

**Table 5.2: Mean, max, and RMSE errors of fitting stair distance and sphere diameter**

| Speed | Stair/$mm$ | | | Sphere/$mm$ | | |
|---|---|---|---|---|---|---|
| /$mms^{-1}$ | $E_{Mean}$ | $E_{Max}$ | $E_{RMSE}$ | $E_{Mean}$ | $E_{Max}$ | $E_{RMSE}$ |
| 0 | 0.0834 | 0.1086 | 0.0845 | 0.091 | 0.0981 | 0.0921 |
| 100 | 0.2487 | 0.4034 | 0.2624 | 0.2864 | 0.3638 | 0.2902 |
| 200 | 0.4368 | 0.5427 | 0.4456 | 0.3417 | 0.3921 | 0.3346 |
| 500 | 0.3902 | 0.5993 | 0.4036 | 0.3852 | 0.4452 | 0.3879 |
| 1000 | 0.4756 | 0.5727 | 0.4867 | 0.4425 | 0.5177 | 0.4458 |

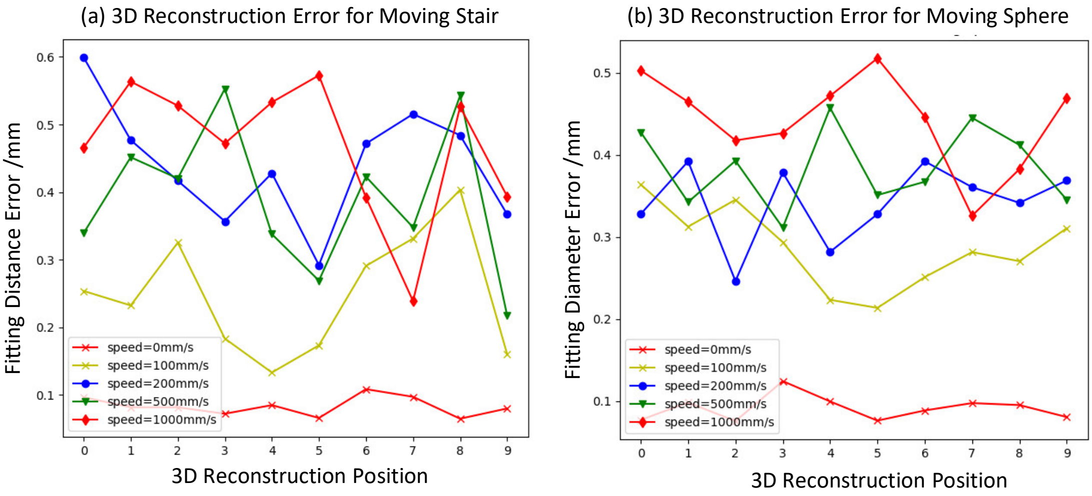

**Figure 5.9: 3D reconstruction error of the moving object at different speeds. (a) 3D reconstruction error of the stair. (b) 3D reconstruction error of the sphere.**

Experimental results demonstrate that the system maintains a high level of measurement accuracy for moving objects, comparable to the accuracy achieved with stationary objects, thereby underscoring its efficacy in measuring moving objects. Moreover, the method's versatility extends its applicability beyond traditional uses. It can enhance camera-projector systems by expanding their reconstruction range and resolving synchronization issues between the projection pattern and the object's motion through visual feedback. This versatility signifies the system's potential for broader applicability in various domains, including industrial inspection, where it could be used for scanning and 3D reconstruction of products freely placed on production lines during transit, thereby improving production efficiency. The system can be also applied in motion analysis, aiding in detailed studies of object movement. In robotics, this technology could be instrumental for navigating and grasping moving objects. Furthermore, in virtual reality, the system could be used to capture dynamic 3D models of objects or for interactive experiences.

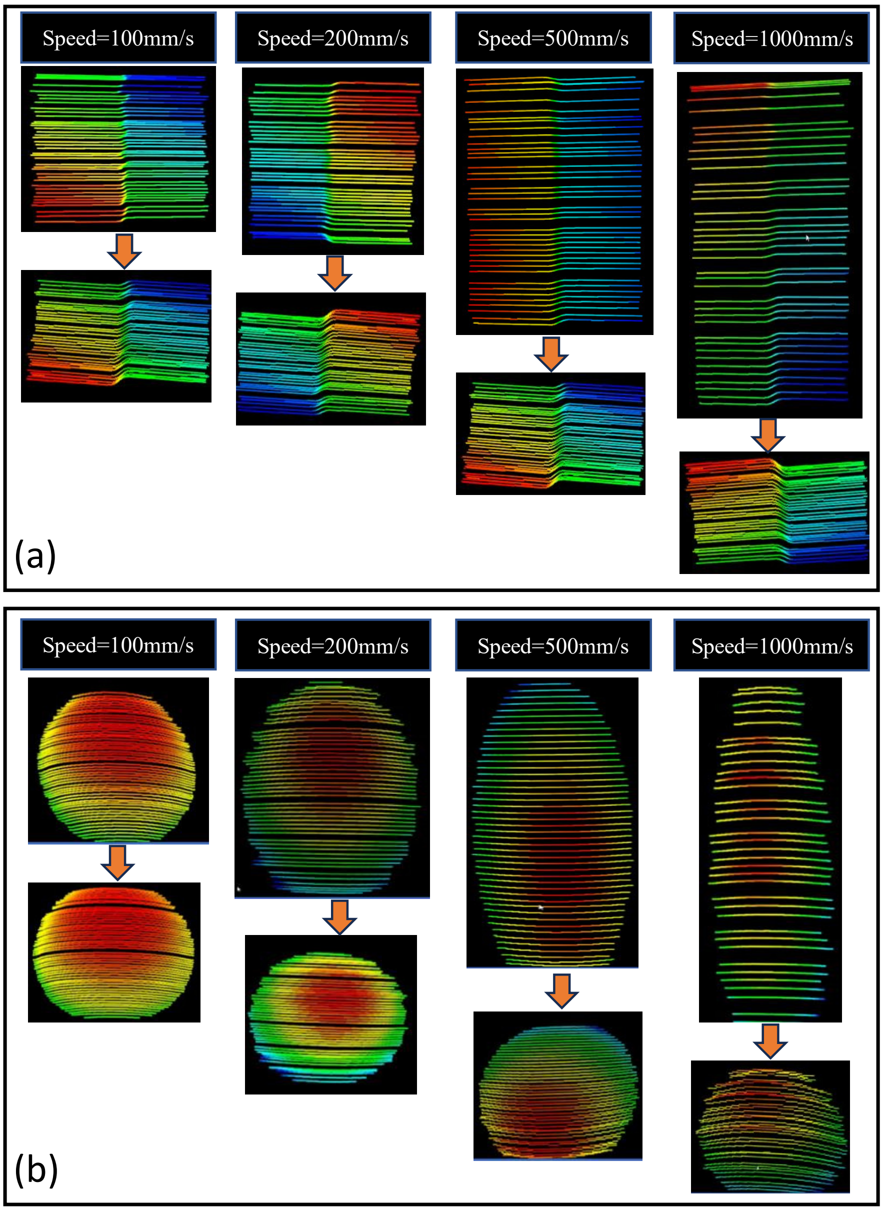

**Figure 5.10: 3D movement compensation results at different speeds. (a) The 3D point clouds of the stair before and after compensation. (b) The 3D point clouds of the sphere before and after compensation.**

# Chapter 6

# Conclusions

In this study, we proposed a novel active 3D reconstruction method for high-speed moving objects that can achieve real-time tracking of objects and feedback the motion information to a 3D system to keep the moving object stationary relative to the 3D system. This is accomplished through a tri-galvanometer based active camera-projector system, enabling high-precision 3D reconstruction.

This research comprises two main components. The first is the development of an active 3D reconstruction system to address the limited 3D reconstruction range issue. The second component builds upon the first by incorporating a visual feedback system, which resolves the synchronization issues between the moving target and the projection.

To realize wide-range 3D sensing, this study presents a novel method that synchronizes laser scanning by switching the field-of-view (FOV) of a camera using multiple galvanometers. Beyond the advanced hardware setup, we established a comprehensive geometric model of the system by modeling the dynamic camera, dynamic laser, and their combined interaction. Furthermore, since existing calibration methods mainly focus on either dynamic lasers or dynamic cameras and have certain limitations, we proposed a novel high-precision and flexible calibration method by constructing an error model and minimizing the objective function.

The performance of the proposed method was evaluated by scanning standard components. The results show that the proposed 3D reconstruction system achieves an accuracy of 0.3 mm when the measurement range is extended to 1100 mm × 1300 mm × 650 mm. This demonstrates that for meter-scale reconstruction ranges, sub-millimeter measurement accuracy is achieved, indicating that the proposed method realizes multi-scale 3D reconstruction and simultaneously allows for high-precision and wide-range 3D reconstruction in industrial applications.

A dynamic light-section 3D reconstruction system is proposed in this study, which overcomes the trade-off between accuracy and measurement range by using multiple galvanometers. A geometric model of the system is established, and a flexible and accurate calibration method is developed. The experimental results demonstrate that the proposed system performs well in terms of measurements, indicating its potential for industrial applications where high-precision and wide-range 3D reconstruction is required. Furthermore, the proposed method can be used in conjunction with the active tracking system for 3D reconstruction of moving targets. This will be introduced in our other work.

To overcome the motion issue in 3D reconstruction, this paper introduces an innovative approach that synergistically combines tracking and active 3D reconstruction tailored for moving objects. By integrating visual feedback derived from tracking outcomes, the proposed system ensures that the object maintains a relatively stable relationship with the 3D reconstruction process throughout its movement. The hardware configuration facilitates simultaneous control of tracking, laser scanning, and 3D reconstruction. A comprehensive mathematical model is established to encompass the tracking, active 3D reconstruction, and 3D motion compensation. Furthermore, a precise calibration method based on this mathematical model is detailed.

Experiments indicate the effectiveness of the proposed method. Specifically, for objects moving at 1000 mm/s, our system achieves a 3D reconstruction accuracy of 0.5 mm, comparable to scenarios with stationary objects. This suggests that our method is promising for high-quality 3D reconstruction of moving objects, enhancing the potential of laser scanning systems for applications such as motion analysis, real-time industrial inspections, and robotic interactions. The novel 3D reconstruction method based on the light-section technique integrates visual feedback from tracking results to ensure the object remains stationary relative to the 3D reconstruction system during movement. A comprehensive mathematical model of the system is established, and a flexible and accurate calibration method is developed. Experimental results demonstrate that the system maintains a high level of measurement accuracy for moving objects, comparable to the accuracy achieved with stationary objects, thereby underscoring its efficacy in measuring moving objects.

For future work, improving the speed of the current system can further enhance the reconstruction accuracy of moving targets. The line laser in the existing system can also be replaced with a projector to achieve active 3D reconstruction based on structured light.

The versatility of the proposed method extends its applicability beyond traditional uses. It can enhance camera-projector systems by expanding their reconstruction range and resolving synchronization issues between the projection pattern and the object's motion through visual feedback. This versatility signifies the system's potential for broader applicability in various domains, including industrial inspection, where it could be used for scanning and 3D reconstruction of products freely placed on production lines during transit, thereby improving production efficiency. The system can also be applied in motion analysis, aiding in detailed studies of object movement. In robotics, this technology could be instrumental for navigating and grasping moving objects. Furthermore, in virtual reality, the system could be used to capture dynamic 3D models of objects or for interactive experiences.

[1] Z. Ma and S. Liu, “A review of 3d reconstruction techniques in civil engineering and their applications,” *Advanced Engineering Informatics*, vol. 37, pp. 163–174, 2018.

[2] V. K. Reja, K. Varghese, and Q. P. Ha, “Computer vision-based construction progress monitoring,” *Automation in Construction*, vol. 138, p. 104245, 2022.

[3] B. Fei, W. Yang, W.-M. Chen, Z. Li, Y. Li, T. Ma, X. Hu, and L. Ma, “Comprehensive review of deep learning-based 3d point cloud completion processing and analysis,” *IEEE Transactions on Intelligent Transportation Systems*, vol. 23, no. 12, pp. 22 862–22 883, 2022.

[4] J. Butime, I. Gutierrez, L. G. Corzo, and C. F. Espronceda, “3d reconstruction methods, a survey,” in *Proceedings of the First International Conference on Computer Vision Theory and Applications*, pp. 457–463, 2006.

[5] L. Gomes, O. R. P. Bellon, and L. Silva, “3d reconstruction methods for digital preservation of cultural heritage: A survey,” *Pattern Recognition Letters*, vol. 50, pp. 3–14, 2014.

[6] C. Griwodz, S. Gasparini, L. Calvet, P. Gurdjos, F. Castan, B. Maujean, G. De Lillo, and Y. Lanthony, “Alicevision meshroom: An open-source 3d reconstruction pipeline,” in *Proceedings of the 12th ACM multimedia systems conference*, pp. 241–247, 2021.

[7] H. Ham, J. Wesley, and H. Hendra, “Computer vision based 3d reconstruction: A review,” *International Journal of Electrical and Computer Engineering*, vol. 9, no. 4, p. 2394, 2019.

[8] Y. Jin, D. Jiang, and M. Cai, “3d reconstruction using deep learning: a survey,” *Communications in Information and Systems*, vol. 20, no. 4, pp. 389–413, 2020.

[9] M. Keller, D. Lefloch, M. Lambers, S. Izadi, T. Weyrich, and A. Kolb, “Real-time 3d reconstruction in dynamic scenes using point-based fusion,” in *2013 International Conference on 3D Vision-3DV 2013*, pp. 1–8. IEEE, 2013.

[10] F. A. Van den Heuvel, “3d reconstruction from a single image using geometric constraints,” *ISPRS Journal of Photogrammetry and Remote Sensing*, vol. 53, no. 6, pp. 354–368, 1998.

[11] R.-J. Li, K.-C. Fan, Q.-X. Huang, H. Zhou, E.-M. Gong, and M. Xiang, “A long-stroke 3d contact scanning probe for micro/nano coordinate measuring machine,” *Precision Engineering*, vol. 43, pp. 220–229, 2016.

[12] Y. Wei, Z. Ding, H. Huang, C. Yan, J. Huang, and J. Leng, “A non-contact measurement method of ship block using image-based 3d reconstruction technology,” *Ocean Engineering*, vol. 178, pp. 463–475, 2019.

[13] S. Bhat and D. Smith, “Laser and sound scanner for non-contact 3d volume measurement and surface texture analysis,” *Physiological Measurement*, vol. 15, no. 1, p. 79, 1994.

[14] J. McBride and C. Maul, “The 3d measurement and analysis of high precision surfaces using con-focal optical methods,” *IEICE transactions on electronics*, vol. 87, no. 8, pp. 1261–1267, 2004.

[15] I. Goda, G. L’Hostis, and P. Guerlain, “In-situ non-contact 3d optical deformation measurement of large capacity composite tank based on close-range photogrammetry,” *Optics and Lasers in Engineering*, vol. 119, pp. 37–55, 2019.

[16] S. Haidacher and G. Hirzinger, “Estimating finger contact location and object pose from contact measurements in 3d grasping,” in *2003 IEEE International Conference*

*on Robotics and Automation (Cat. No. 03CH37422)*, vol. 2, pp. 1805–1810. IEEE, 2003.

[17] X. Su and Q. Zhang, “Dynamic 3-d shape measurement method: a review,” *Optics and Lasers in Engineering*, vol. 48, no. 2, pp. 191–204, 2010.

[18] M. Aharchi and M. Ait Kbir, “A review on 3d reconstruction techniques from 2d images,” in *Innovations in Smart Cities Applications Edition 3: The Proceedings of the 4th International Conference on Smart City Applications 4*, pp. 510–522. Springer, 2020.

[19] J.-J. Aguilar, F. Torres, and M. Lope, “Stereo vision for 3d measurement: accuracy analysis, calibration and industrial applications,” *Measurement*, vol. 18, no. 4, pp. 193–200, 1996.

[20] P. N. B. Do and Q. C. Nguyen, “A review of stereo-photogrammetry method for 3-d reconstruction in computer vision,” in *2019 19th International Symposium on Communications and Information Technologies (ISCIT)*, pp. 138–143. IEEE, 2019.

[21] A. Geiger, J. Ziegler, and C. Stiller, “Stereoscan: Dense 3d reconstruction in real-time,” in *2011 IEEE intelligent vehicles symposium (IV)*, pp. 963–968. Ieee, 2011.

[22] S. Á. Gumundsson, M. Pardas, J. R. Casas, J. R. Sveinsson, H. Aanæs, and R. Larsen, “Improved 3d reconstruction in smart-room environments using tof imaging,” *Computer Vision and Image Understanding*, vol. 114, no. 12, pp. 1376–1384, 2010.

[23] C. Kerl, M. Souiai, J. Sturm, and D. Cremers, “Towards illumination-invariant 3d reconstruction using tof rgb-d cameras,” in *2014 2nd International Conference on 3D Vision*, vol. 1, pp. 39–46. IEEE, 2014.

[24] W. Xie, S. Wei, and D. Yang, “Morphological measurement for carrot based on three-dimensional reconstruction with a tof sensor,” *Postharvest Biology and Technology*, vol. 197, p. 112216, 2023.

[25] C. Albitar, P. Graebling, and C. Doignon, “Robust structured light coding for 3d reconstruction,” in *2007 IEEE 11th international conference on computer vision*, pp. 1–6. IEEE, 2007.

[26] S. Zhang, “High-speed 3d shape measurement with structured light methods: A review,” *Optics and lasers in engineering*, vol. 106, pp. 119–131, 2018.

[27] E. Lilienblum and A. Al-Hamadi, “A structured light approach for 3-d surface reconstruction with a stereo line-scan system,” *IEEE Transactions on Instrumentation and Measurement*, vol. 64, no. 5, pp. 1258–1266, 2015.

[28] Z. Liu, X. Liu, Z. Cao, X. Gong, M. Tan, and J. Yu, “High precision calibration for three-dimensional vision-guided robot system,” *IEEE Transactions on Industrial Electronics*, vol. 70, no. 1, pp. 624–634, 2022.

[29] Y. Liu, P. Sun, and A. Namiki, “Target tracking of moving and rotating object by high-speed monocular active vision,” *IEEE Sensors Journal*, vol. 20, no. 12, pp. 6727–6744, 2020.

[30] K. Shimada, A. Namiki, and I. Ishii, “High-speed 3-d measurement of a moving object with visual servo,” in *2016 IEEE/SICE International Symposium on System Integration (SII)*, pp. 248–253. IEEE, 2016.

[31] R. Deng, X. Jin, and D. Du, “3d location and trajectory reconstruction of a moving object behind scattering media,” *IEEE Transactions on Computational Imaging*, vol. 8, no. 10, pp. 371–384, 2022.

[32] D. Iwai, K. Kodama, and K. Sato, "Reducing motion blur artifact of foveal projection for a dynamic focus-plus-context display," *IEEE Transactions on Circuits and Systems for Video Technology*, vol. 25, no. 4, pp. 547–556, 2014.

[33] T. Jun, "Face reconstruction based on camera-projector system," in *2012 International Conference on Industrial Control and Electronics Engineering*, pp. 1026–1029. IEEE, 2012.

[34] J. W. Horbach and T. Dang, "3d reconstruction of specular surfaces using a calibrated projector–camera setup," *Machine Vision and Applications*, vol. 21, pp. 331–340, 2010.

[35] Q. Zeng, C. Yang, D. Tang, J. Li, Z. Feng, J. Liu, and K. Guan, "Additive manufacturing alumina components with lattice structures by digital light processing technique," *Journal of Materials Science & Technology*, vol. 35, no. 12, pp. 2751–2755, 2019.

[36] F. Sadlo, T. Weyrich, R. Peikert, and M. Gross, "A practical structured light acquisition system for point-based geometry and texture," in *Proceedings Eurographics/IEEE VGTC Symposium Point-Based Graphics, 2005.*, pp. 89–145. IEEE, 2005.

[37] C. Rocchini, P. Cignoni, C. Montani, P. Pingi, and R. Scopigno, "A low cost 3d scanner based on structured light," in *computer graphics forum*, vol. 20, no. 3, pp. 299–308. Wiley Online Library, 2001.

[38] X. Xu, Z. Fei, J. Yang, Z. Tan, and M. Luo, "Line structured light calibration method and centerline extraction: A review," *Results in Physics*, vol. 19, p. 103637, 2020.

[39] B. Cui, W. Tao, and H. Zhao, "High-precision 3d reconstruction for small-to-medium-sized objects utilizing line-structured light scanning: A review," *Remote Sensing*, vol. 13, no. 21, p. 4457, 2021.

[40] Q. Tang, C. Liu, Z. Cai, H. Zhao, X. Liu, and X. Peng, “An improved spatiotemporal correlation method for high-accuracy random speckle 3d reconstruction,” *Optics and Lasers in Engineering*, vol. 110, pp. 54–62, 2018.

[41] H. Nguyen, T. Tran, Y. Wang, and Z. Wang, “Three-dimensional shape reconstruction from single-shot speckle image using deep convolutional neural networks,” *Optics and Lasers in Engineering*, vol. 143, p. 106639, 2021.

[42] J. Cheng, D. Tao, Y. Quan, D. W. K. Wong, G. C. M. Cheung, M. Akiba, and J. Liu, “Speckle reduction in 3d optical coherence tomography of retina by a-scan reconstruction,” *IEEE transactions on medical imaging*, vol. 35, no. 10, pp. 2270–2279, 2016.

[43] H. Anwar, I. Din, and K. Park, “Projector calibration for 3d scanning using virtual target images,” *International Journal of Precision Engineering and Manufacturing*, vol. 13, pp. 125–131, 2012.

[44] Z. Song and R. Chung, “Use of lcd panel for calibrating structured-light-based range sensing system,” *IEEE Transactions on Instrumentation and Measurement*, vol. 57, no. 11, pp. 2623–2630, 2008.

[45] Y. Yin, X. Peng, A. Li, X. Liu, and B. Z. Gao, “Calibration of fringe projection profilometry with bundle adjustment strategy,” *Optics letters*, vol. 37, no. 4, pp. 542–544, 2012.

[46] W. Zhang, W. Li, L. Yu, H. Luo, H. Zhao, and H. Xia, “Sub-pixel projector calibration method for fringe projection profilometry,” *Optics express*, vol. 25, no. 16, pp. 19 158–19 169, 2017.

[47] J. Liu, X. Yu, K. Yang, X. Zhu, and Y. Wu, “Automatic calibration method for the

full parameter of a camera-projector system," *Optical Engineering*, vol. 58, no. 8, pp. 084 105–084 105, 2019.

[48] Q. Yuan, J. Wu, H. Zhang, J. Yu, and Y. Ye, "Unsupervised-learning-based calibration method in microscopic fringe projection profilometry," *Applied Optics*, vol. 62, no. 27, pp. 7299–7315, 2023.

[49] S. M. M. Gazafrudi, D. Younesian, and M. Torabi, "A high accuracy and high speed imaging and measurement system for rail corrugation inspection," *IEEE Transactions on Industrial Electronics*, vol. 68, no. 9, pp. 8894–8903, 2021.

[50] Y.-j. Zhao, Y.-x. Xiong, and Y. Wang, "Three-dimensional accuracy of facial scan for facial deformities in clinics: a new evaluation method for facial scanner accuracy," *PLoS One*, vol. 12, no. 1, p. e0169402, Jan. 2017.

[51] C. Wei, C. Sihai, L. Dong, and J. Guohua, "A compact two-dimensional laser scanner based on piezoelectric actuators," *Review of Scientific Instruments*, vol. 86, no. 1, p. 013102, Jan. 2015.

[52] A. Wan, Y. Wang, G. Xue, K. Chen, and J. Xu, "Accurate kinematics calibration method for a large-scale machine tool," *IEEE Transactions on Industrial Electronics*, vol. 68, no. 10, pp. 9832–9843, 2021.

[53] X. Lü, D. Gu, Y. Wang, Y. Qu, C. Qin, and F. Huang, "Feature extraction of welding seam image based on laser vision," *IEEE Sensors Journal*, vol. 18, no. 11, pp. 4715–4724, Jun. 2018.

[54] S. Yoon, Y. Son, S.-y. Oh, and S. Han, "A distortion model of laser sheet for a laser line scanner with large fan angle," *IEEE Transactions on Industrial Electronics*, vol. 67, no. 8, pp. 6986–6995, Aug. 2020.

[55] X. Du and Q. Chen, “Dual-laser goniometer: A flexible optical angular sensor for joint angle measurement,” *IEEE Transactions on Industrial Electronics*, vol. 68, no. 7, pp. 6328–6338, 2021.

[56] B. Deng, W. Wu, X. Li, H. Wang, Y. He, G. Shen, Y. Tang, K. Zhou, Z. Zhang, and Y. Wang, “Active 3-d thermography based on feature-free registration of thermogram sequence and 3-d shape via a single thermal camera,” *IEEE Transactions on Industrial Electronics*, vol. 69, no. 11, pp. 11 774–11 784, 2022.

[57] X. Xu, Z. Fei, J. Yang, Z. Tan, and M. Luo, “Line structured light calibration method and centerline extraction: A review,” *Results in Physics*, vol. 19, no. 3, p. 103637, Dec. 2020.

[58] J. Xiao, X. Hu, W. Lu, J. Ma, and X. Guo, “A new three-dimensional laser scanner design and its performance analysis,” *Optik*, vol. 126, no. 7-8, pp. 701–707, Apr. 2015.

[59] E. Lilienblum and A. Al-Hamadi, “A structured light approach for 3-d surface reconstruction with a stereo line-scan system,” *IEEE Transactions on Instrumentation and Measurement*, vol. 64, no. 5, pp. 1258–1266, 2015.

[60] C. Wang and J. Zeng, “Combination-chord measurement of rail corrugation using triple-line structured-light vision: Rectification and optimization,” *IEEE Transactions on Intelligent Transportation Systems*, vol. 22, no. 11, pp. 7256–7265, 2021.

[61] Y. Li, J. Zhou, Q. Mao, J. Jin, and F. Huang, “Line structured light 3d sensing with synchronous color mapping,” *IEEE Sensors Journal*, vol. 20, no. 17, pp. 9796–9805, 2020.

[62] S. Yin, Y. Ren, Y. Guo, J. Zhu, S. Yang, and S. Ye, “Development and calibration

of an integrated 3d scanning system for high-accuracy large-scale metrology," *Measurement*, vol. 54, no. 9, pp. 65–76, Aug. 2014.

[63] D. Wertjanz, E. Csencsics, T. Kern, and G. Schitter, "Bringing the lab to the fab: Robot-based inline measurement system for precise 3-d surface inspection in vibrational environments," *IEEE Transactions on Industrial Electronics*, vol. 69, no. 10, pp. 10 666–10 673, 2022.

[64] X. Liu, H. Madhusudanan, W. Chen, D. Li, J. Ge, C. Ru, and Y. Sun, "Fast eye-in-hand 3-d scanner-robot calibration for low stitching errors," *IEEE Transactions on Industrial Electronics*, vol. 68, no. 9, pp. 8422–8432, 2021.

[65] H. Xie, W. Li, and H. Liu, "General geometry calibration using arbitrary free-form surface in a vision-based robot system," *IEEE Transactions on Industrial Electronics*, vol. 69, no. 6, pp. 5994–6003, 2022.

[66] L. Yang, E. Li, T. Long, J. Fan, and Z. Liang, "A novel 3-d path extraction method for arc welding robot based on stereo structured light sensor," *IEEE Sensors Journal*, vol. 19, no. 2, pp. 763–773, 2019.

[67] T. Jiang, H. Cui, and X. Cheng, "Accurate calibration for large-scale tracking-based visual measurement system," *IEEE Transactions on Instrumentation and Measurement*, vol. 70, pp. 1–11, Aug. 2021.

[68] F. Han, Q. Zhang, B. Fu, T. Yang, Y. Wang, and R. Xiong, "Multiconstraint spatial and temporal calibration of rotating line structured light vision sensor," *IEEE Transactions on Instrumentation and Measurement*, vol. 70, pp. 1–11, 2021.

[69] C. Gu, Y. Cong, and G. Sun, "Three birds, one stone: Unified laser-based 3-d reconstruction across different media," *IEEE Transactions on Instrumentation and Measurement*, vol. 70, pp. 1–12, 2021.

[70] A. Wan, Y. Wang, G. Xue, K. Chen, and J. Xu, "Accurate kinematics calibration method for a large-scale machine tool," *IEEE Transactions on Industrial Electronics*, vol. 68, no. 10, pp. 9832–9843, 2021.

[71] T. Fang, J. An, Q. Chen, Y. He, H. Wang, and X. Zhang, "Progress and comparison in nondestructive detection, imaging and recognition technology for defects of wafers, chips and solder joints," *Nondestructive Testing and Evaluation*, pp. 1–56, 2023.

[72] S. L. Y. Y. P. H. T. L. S. J. Teng Wang, Shuming Yang, "Error analysis and compensation of galvanometer laser scanning measurement system," *Acta Optica Sinica*, vol. 40, pp. 1–13, 2020.

[73] P. Eisert, K. Polthier, and J. Hornegger, "A mathematical model and calibration procedure for galvanometric laser scanning systems," in *Vision, Modeling, and Visualization*, vol. 591, pp. 207–214, 12 2011.

[74] C. Yu, X. Chen, and J. Xi, "Modeling and calibration of a novel one-mirror galvanometric laser scanner," *Sensors*, vol. 17, no. 1, p. 164, Jan. 2017.

[75] S. Yang, L. Yang, G. Zhang, T. Wang, and X. Yang, "Modeling and calibration of the galvanometric laser scanning three-dimensional measurement system," *Nanomanufacturing and Metrology*, vol. 1, no. 3, pp. 180–192, Sep. 2018.

[76] X. Li, B. Liu, X. Mei, W. Wang, X. Wang, and X. Li, "Development of an in-situ laser machining system using a three-dimensional galvanometer scanner," *Engineering*, vol. 6, no. 1, pp. 68–76, 2020.

[77] X. Zexiao, W. Jianguo, and J. Ming, "Study on a full field of view laser scanning system," *International Journal of Machine Tools and Manufacture*, vol. 47, no. 1, pp. 33–43, 2007.

[78] S. Chi, Z. Xie, and W. Chen, “A laser line auto-scanning system for underwater 3d reconstruction,” *Sensors*, vol. 16, no. 9, p. 1534, 2016.

[79] M. Chen, Q. Li, K. Shimasaki, S. Hu, Q. Gu, and I. Ishii, “A novel dynamic light-section 3d reconstruction method for wide-range sensing,” 2024.

[80] W. Flores-Fuentes, G. Trujillo-Hernández, I. Y. Alba-Corpus, J. C. Rodríguez-Quiñonez, J. E. Mirada-Vega, D. Hernández-Balbuena, F. N. Murrieta-Rico, and O. Sergiyenko, “3d spatial measurement for model reconstruction: A review,” *Measurement*, vol. 207, p. 112321, 2023.

[81] Y. Li and Z. Wang, “3d reconstruction with single-shot structured light rgb line pattern,” *Sensors*, vol. 21, no. 14, p. 4819, 2021.

[82] B. Wen, J. Tremblay, V. Blukis, S. Tyree, T. Müller, A. Evans, D. Fox, J. Kautz, and S. Birchfield, “Bundlesdf: Neural 6-dof tracking and 3d reconstruction of unknown objects,” in *Proceedings of the IEEE/CVF Conference on Computer Vision and Pattern Recognition*, pp. 606–617, 2023.

[83] M. Duan, Y. Jin, H. Chen, J. Zheng, C. Zhu, and E. Chen, “Automatic 3-d measurement method for nonuniform moving objects,” *IEEE Transactions on Instrumentation and Measurement*, vol. 70, pp. 1–11, 2021.

[84] Z. Qinghui, L. Hao, L. Lei, L. Shenglin, and P. Wei, “3d reconstruction of the moving object with double-shooting based on phase shifting profilometry,” *Infrared an Laser Engineering*, vol. 52, no. 12, pp. 20 220 891–1, 2023.

[85] M. Maruyama, S. Tabata, Y. Watanabe, and M. Ishikawa, “Multi-pattern embedded phase shifting using a high-speed projector for fast and accurate dynamic 3d measurement,” in *2018 IEEE winter conference on applications of computer vision (WACV)*, pp. 921–929. IEEE, 2018.

[86] A. Namiki, K. Shimada, Y. Kin, and I. Ishii, “Development of an active high-speed 3-d vision system,” *Sensors*, vol. 19, no. 7, p. 1572, 2019.

[87] F. Blais, M. Picard, and G. Godin, “Accurate 3d acquisition of freely moving objects,” in *2nd International Symposium on 3D Data Processing, Visualization and Transmission*, pp. 422–429, Oct. 2004.

[88] S. Goel and B. Lohani, “A motion correction technique for laser scanning of moving objects,” *IEEE geoscience and remote sensing letters*, vol. 11, no. 1, pp. 225–228, 2013.

[89] X. Ying, K. Peng, Y. Hou, S. Guan, J. Kong, and H. Zha, “Self-calibration of catadioptric camera with two planar mirrors from silhouettes,” *IEEE Transactions on Pattern Analysis and Machine Intelligence*, vol. 35, no. 5, pp. 1206–1220, May. 2013.

[90] Z. Wu and R. J. Radke, “Keeping a pan-tilt-zoom camera calibrated,” *IEEE Transactions on Pattern Analysis and Machine Intelligence*, vol. 35, no. 8, pp. 1994–2007, Aug. 2013.

[91] G. A.-C. J. P. S. Adam Schmidt, Li Sun, “The calibration of the pan-tilt units for the active stereo head,” in *Vision, Modeling, and Visualization*, vol. 389, pp. 213–221, Oct. 2016.

[92] I. N. Junejo and H. Foroosh, “Optimizing ptz camera calibration from two images,” *Machine Vision and Applications*, vol. 23, no. 2, pp. 375–389, Feb. 2012.

[93] S. Kumar, C. Micheloni, C. Piciarelli, and G. L. Foresti, “Stereo rectification of uncalibrated and heterogeneous images,” *Pattern Recognition Letters*, vol. 31, no. 11, pp. 1445–1452, Aug. 2010.

[94] Z. Han and L. Zhang, “Modeling and calibration of a galvanometer-camera imaging system,” *IEEE Transactions on Instrumentation and Measurement*, vol. 71, pp. 1–9, 2022.

[95] S. Hu, Y. Matsumoto, T. Takaki, and I. Ishii, “Monocular stereo measurement using high-speed catadioptric tracking,” *Sensors*, vol. 17, no. 8, p. 1839, Aug. 2017.

# Acknowledgment

First of all, I would like to express my deep gratitude to my advisor,**Prof. Idaku Ishii**. Prof. Ishii provided comprehensive advice that guided me step by step from a new researcher to where I am now. I have learned immensely from each meeting with Prof. Ishii, and I am consistently awed by his vast knowledge and profound thinking. He can always pinpoint the core issues immediately and offer invaluable advice that reflects his exceptional research and teaching skills. Prof. Ishii's research philosophy has helped me redefine my understanding of meaningful research and how to advance it systematically. Moreover, he has always been kind and supportive, offering me significant assistance in my daily life. I am eternally grateful to Prof. Ishii, and it has been my great fortune to have his guidance throughout my PhD journey.

I would also like to thank **Dr. Feiyue Wang**, **Dr. Kohei Shimasaki** and **Dr. Shaopeng Hu**, who assisted me in completing my experiments when I had to conduct remote research. My thanks extend to **Dr. Qing Li**, **Dr. Wenxiang Qin**, and **Dr. Hongyu Dong**, who have always been by my side, bringing much joy into my life.

I am very grateful to **Ms. Yukari Kaneyuki** and **Ms. Michiko Kanzaki**. You both helped me navigate many procedural challenges during my PhD. Despite the complexity of many tasks, you always remained kind and patient, assisting me repeatedly. I will always remember your smiles fondly.

I want to express my sincere thanks to the bachelor and master students in the Robotics Laboratory. You provided me with valuable connections not only in research but also in life.

I am also grateful to the staff at Hiroshima University and the Japanese government for providing me with the scholarship and environment that were crucial for my research and life in Japan.

I would like to thank my parents for their silent support and encouragement, which allowed me to focus on my studies without worry.

Finally, I sincerely wish health and happiness to all the people I love and to all those who love me.

May, 2024
Chen Mengjuan